

# REPORT DOCUMENTATION PAGE

Form Approved  
OMB No. 0704-0188

Public reporting burden for this collection of information is estimated to average 1 hour per response, including the time for reviewing instructions, searching existing data sources, gathering and maintaining the data needed, and completing and reviewing the collection of information. Send comments regarding this burden estimate or any other aspect of this collection of information, including suggestions for reducing this burden, to Washington Headquarters Services, Directorate for Information Operations and Reports, 1215 Jefferson Davis Highway, Suite 1204, Arlington, VA 22202-4302, and to the Office of Management and Budget, Paperwork Reduction Project (0704-0188), Washington, DC 20503.

1. AGENCY USE ONLY (Leave blank)			2. REPORT DATE 1/99		3. REPORT TYPE AND DATES COVERED Final Technical Report 6/92-12/98		
4. TITLE AND SUBTITLE  Growth of InTlSb and InTlP for Long Wavelength Infrared Detector Applications			5. FUNDING NUMBERS  N00014-92-J-1951				
6. AUTHOR(S)  M. Razeghi							
7. PERFORMING ORGANIZATION NAME(S) AND ADDRESS(ES)  Northwestern University Center for Quantum Devices 2225 N. Campus Drive MLSB Room 4051 Evanston, IL 60208-3219			8. PERFORMING ORGANIZATION REPORT NUMBER  0650-350-F451				
9. SPONSORING / MONITORING AGENCY NAME(S) AND ADDRESS(ES)  Office of Naval Research 800 N. Quincy Street Arlington, VA 22217-5660			10. SPONSORING / MONITORING AGENCY REPORT NUMBER				
11. SUPPLEMENTARY NOTES							
12a. DISTRIBUTION / AVAILABILITY STATEMENT  Approved for public release; distribution unlimited					12b. DISTRIBUTION CODE		
The objective of this research is to develop room temperature operating long-wavelength infrared (LWIR) photodetectors with novel III-V alloys. For the first time, we have successfully demonstrated the growth of InTlSb, InTlP, and InTlAsSb alloys by low-pressure metalorganic chemical vapor deposition. Other novel alloys such as InAsSb and InSbBi are also investigated. The structural, optical, and electrical properties of these novel materials have been investigated in detail with various <i>ex-situ</i> characterization techniques.							
For the first time, preliminary LWIR InTlSb photodetectors on GaAs are fabricated with the grown materials and device performance has been characterized. The InTlSb photoconductor showed 11 μm cutoff wavelength at room temperature. The Johnson-noise limited detectivity is estimated to be in the range of $10^6$ - $10^7$ cmHz $^{1/2}$ /W. The carrier lifetime is derived from the voltage-dependent responsivity, which is in 0.1-0.6 ns at 300 K.							
Photoconductivity measurements on InTlP/InP indicate an increase of the cutoff wavelength up to 8 μm with increasing Tl incorporation. Recently, we have observed LWIR photoconductivity up to 15 μm at room temperature by incorporating Tl into InAsSb. These results clearly show the feasibility of using III-V alloys for LWIR photodetector applications as an alternative to HgCdTe detectors.					15. NUMBER OF PAGES 45		
14. SUBJECT TERMS					16. PRICE CODE		
17. SECURITY CLASSIFICATION OF REPORT		18. SECURITY CLASSIFICATION OF THIS PAGE		19. SECURITY CLASSIFICATION OF ABSTRACT		20. LIMITATION OF ABSTRACT	

# **Growth of InTlSb and InTlP for Long Wavelength Infrared Detector Applications**

Contract No. N00014-92-J-1951

**Project Manager : Dr. George Wright/Dr. Yoon-Soo Park**

**Principal Investigator: Dr. Manijeh Razeghi**

**Center for Quantum Devices  
Dept. of Electrical and Computer Engineering  
Northwestern University  
Evanston, Illinois 60208**

**1990126 061**

## ABSTRACT

The objective of this research is to develop room temperature operating long-wavelength infrared (LWIR) photodetectors with novel III-V alloys. For the first time, we have successfully demonstrated the growth of InTlSb, InTlP, and InTlAsSb alloys by low-pressure metalorganic chemical vapor deposition. Other novel alloys such as InAsSb and InSbBi are also investigated. The structural, optical, and electrical properties of these novel materials have been investigated in detail with various *ex-situ* characterization techniques.

For the first time, preliminary LWIR InTlSb photodetectors on GaAs are fabricated with the grown materials and device performance has been characterized. The InTlSb photoconductor showed 11  $\mu\text{m}$  cutoff wavelength at room temperature. The Johnson-noise limited detectivity is estimated to be in the range of  $10^6$ - $10^7 \text{ cmHz}^{1/2}/\text{W}$ . The carrier lifetime is derived from the voltage-dependent responsivity, which is in 0.1-0.6 ns at 300 K.

Photoconductivity measurements on InTlP/InP indicate an increase of the cutoff wavelength up to 8  $\mu\text{m}$  with increasing Tl incorporation. Recently, we have observed LWIR photoconductivity up to 15  $\mu\text{m}$  at room temperature by incorporating Tl into InAsSb. These results clearly show the feasibility of using III-V alloys for LWIR photodetector applications as an alternative to HgCdTe detectors.

## **CONTENTS**

### **INTRODUCTION**

#### **Highlight of the Center for Quantum Devices**

#### **Task 1 Growth of novel III-V materials**

- 1. Growth of high quality InSb**
- 2. Demonstration of the first growth of InTlSb**
- 3. Demonstration of the first growth of InTlP**
- 4. Demonstration of the first growth of InTlAsSb**
- 5. Growth of high quality InSbBi**

#### **Task 2 InTlSb Doping and Contact**

- 6. Doping of InSb, InAsSb, and InTlSb**
- 7. Development of Device Processing Technology**

#### **Task 3 Fabrication of Detectors**

- 8. InTlSb photoconductors on GaAs**
- 9. InAsSb photoconductors on GaAs**
- 10. InSbBi photoconductors on GaAs**
- 11. Photovoltaic detector Performance Measurement**

### **CONCLUSION**

### **REFERENCES**

### **SUMMARY of the PROJECT**

### **LIST OF PUBLICATIONS**

## INTRODUCTION

The objective of this research program is to grow InTlSb and InTlP alloys for long-wavelength infrared detector applications by low-pressure metalorganic chemical vapor deposition (LP-MOCVD) and to investigate their physical properties. As a first step towards this goal, optimum growth conditions for high quality InSb epitaxial films on InSb, GaAs, and Si substrates have been determined. InSb films grown under these conditions exhibited one of the best structural and electrical properties reported so far. For the long-wavelength infrared (LWIR) applications, growth of InTlSb, InTlP, and InTlAsSb were then carried out using arsine, phosphine, and cyclopentadienylthallium as the source for As, P, and Tl respectively. Incorporation of thallium into InSb has led to the first successful growth of InTlSb having an extended infrared response. By changing the thallium flow, thallium content was varied and the resulting absorption edge varied from  $5.5\mu\text{m}$  to  $9.0\mu\text{m}$  at 77 K. The photoconductive detectors have been fabricated and measured using Fourier transform infrared (FTIR) spectrometer and blackbody test setup. Using the Hall data, the effective carrier lifetime and detectivity have been calculated for the InTlSb layers. The spectral responsivity of an InTlSb photoconductor showed  $11\mu\text{m}$  cutoff wavelength at room temperature. The Johnson-noise limited detectivity is estimated to be in the range of  $10^6$ - $10^7\text{ cmHz}^{1/2}/\text{W}$ . The carrier lifetime is derived from the voltage-dependent responsivity, which is in 0.1-0.6 ns at 300 K. Photoconductivity measurements on InTlP/InP indicate an increase of the cutoff wavelength up to  $8\mu\text{m}$  with increasing Tl incorporation. Recently, we have observed LWIR photoconductivity up to  $15\mu\text{m}$  at room temperature by incorporating Tl into InAsSb. These results demonstrate III-V alloys as feasible material systems for LWIR detection.

Efforts of our research have also been devoted to aspects of materials growth related to photovoltaic detector fabrication. Reproducible epitaxial doping, the foremost requirement in realizing photovoltaic detectors, have been first investigated for InSb. Successful n-and p-type doping were obtained using Sn and Zn as the respective dopants, without any observable degradation. Based on this progress, InSb photovoltaic detectors have been fabricated and measured. As a next step, InAsSb photovoltaic detectors have also been fabricated to investigate the doping and detector performance for the InSb based alloy materials. Device processing technology developed at CQD has been used for the fabrication of InSb and InAsSb photovoltaic detectors and will be applied for the InTlSb detectors later. N- and p-type doping of InTlSb were also achieved to a concentration of  $2.5\times 10^{16}\text{cm}^{-3}$  and  $3\times 10^{18}\text{cm}^{-3}$ , respectively. Because lower doping levels are required for the p-type doping, DEZn replaced DMZn for the Zn source. Lower vapor pressure of DEZn resulted in the lower doping level down to  $10^{16}\text{cm}^{-3}$  for InSb and InAsSb

resulting in a better doping level control.

## **Highlights of the Center for Quantum Devices**

The work on developing LWIR detectors at the Center for Quantum Devices began in 1992. Here is the highlight of our achievement as compared to the state of art at that time.

1. Growth of the best (structural and electrical quality) InSb on GaAs substrates. The optimization of the InSb growth condition has been completed.
2. Demonstration of the first growth of InTlSb. Evidenced the incorporation of thallium by Auger Electron Spectroscopy. Observed a shift in the absorption edge by infrared transmission and photoresponse.
3. Varied thallium content and observed the resulting changes in physical properties.
4. Demonstrated InTlSb photoconductors on GaAs with different Tl compositions.  $\text{InTl}_{0.04}\text{Sb}_{0.96}$  photoconductors showed cutoff wavelength of 11  $\mu\text{m}$  at room temperature. The maximum responsivity of  $\text{InTl}_{0.04}\text{Sb}_{0.96}$  photodetector is about 6.64 V/W at 77 K, corresponding to a detectivity of about  $7.64 \times 10^8 \text{ cmHz}^{1/2}/\text{W}$ . The carrier lifetime in InTlSb photodetectors derived from stationary photoconductivity is 10-50 ns at 77 K. Johnson-noise limited detectivity is estimated to be in the range of  $10^6$ - $10^7 \text{ cmHz}^{1/2}/\text{W}$  and the carrier lifetime is in 0.1-0.6 ns at 300 K.
5. Demonstration of the first growth of InTlP. Observed a shift up to 8  $\mu\text{m}$  in the absorption edge by infrared photoresponse.
6. Demonstration of the first growth of InTlAsSb. LWIR photoconductivity up to 15  $\mu\text{m}$  was observed at room temperature.
7. Growth of high quality InSbBi with Bi up to 5 %. Bi incorporation was investigated by energy dispersive x-ray analysis (EDAX), high-resolution x-ray diffraction, Hall measurements, infrared transmission/absorption, and infrared photoresponse measurements.
8. First demonstration of InSbBi photoconductors on GaAs. Johnson-noise limited detectivity at 7  $\mu\text{m}$  was  $4.7 \times 10^8 \text{ cmHz}^{1/2}/\text{W}$  and carrier lifetime was 86 ns at 77 K.
9. First demonstration of room temperature operating 8-12  $\mu\text{m}$  InSbBi photodetector on GaAs.

Johnson-noise limited detectivity at 10.6  $\mu\text{m}$  was  $1.2 \times 10^6 \text{ cmHz}^{1/2}/\text{W}$  and carrier lifetime was 0.7 ns at room temperature.

10. Calibrated the n- and p- type doping level on InSb grown on GaAs using TESn, DMZn and DEZn as dopant sources. Similarity of the doping characteristics for the InAsSb and InTlSb has also been verified.
11. Developed device processing technology such as etching, metallization, and wire bonding for InSb based materials.
12. Demonstrated InSb photovoltaic detectors with different structures (p-i-n and n-i-p). Responsivities have been compared to obtain better structure for the applications.
13. Demonstrated p<sup>+</sup>-p-n<sup>+</sup> InSb/InAsSb/InSb double heterojunction photodiodes operating at 8-13 $\mu\text{m}$  as a step towards the InTlSb photovoltaic detector development.
14. Preliminary InTlSb photovoltaic detector has been attempted.

## **Task 1 Growth of InTlSb**

### **1. Growth of high-quality InSb**

#### Growth

Trimethylindium (TMI) and trimethylantimony (TMSb) were used as precursors. Their respective bubbler temperature were kept at 18° C and 0° C. The growths were carried out on InSb, semi-insulating GaAs, and GaAs coated Si substrate. The latter was investigated because of the possibility for future investigation of infrared detection and signal processing circuits on the same substrates. Superclean GaAs and GaAs/Si substrates were directly loaded into the growth chamber without any preparation. During the heating of the substrate, a pregrowth arsine overpressure was maintained in order to prevent any surface degradation. For InSb substrates, the best preparation method was found to be etching in lactic acid : nitric acid (10:1) mixture. However, we observed that this etching reveals line defects on some InSb substrates. The line defects are believed to originate from the lapping-polishing stages of the substrate preparation.

For the InSb growths, the surface morphology was found to be very sensitive to the V/III ratio and closely reflected the crystallinity of the as-grown films. Based upon the morphology, only a narrow range of V/III ratio around 11 at 465°C was found to be optimum. At a lower V/III ratio around 9, the morphology degraded and the surface was covered with indium droplets; the latter phenomena was confirmed by dissolution of these droplets in hydrochloric acid, which preferentially etches indium. With an increase in V/III ratio the droplets were replaced by hillocks whose density decreased as the ratio reached its optimum value.

Similar studies of the V/III ratio dependence on surface morphology have also been carried out at other temperatures. The optimum condition varied with temperature but similar morphology changes were noticed relative to the optimum point. Optimum V/III ratio increases with decreasing growth temperature. This is due to incomplete decomposition of TMSb at the investigated temperatures. While TMIn completely decomposes around 425°C, TMSb only starts decomposing at 400°C with increasing decomposition efficiency as the temperature increases. hence, higher TMSb flow is required (higher V/III ratio) to compensate for the inefficient decomposition at lower temperatures and as a result, expensive source material is wasted. This might suggest for an increase in the growth temperature but a significant increase is not possible because of the low melting point of InSb (525°C). Growth carried out at temperatures close to the melting point should be avoided since poor quality films are obtained from thermal degradation. Based on these facts and results, the optimum growth temperature and parameters have been determined and they are summarized in Table I

Table I: Optimum growth conditions for InSb

Growth temperature	465°C
Growth pressure	76 Torr
TMIn flow rate	50cc/min
TMSb flow rate	20cc/min
Total H <sub>2</sub> flow rate	1.5 l/min

### Characterization

Under the optimum conditions, mirror-like InSb epilayers were grown on InSb, GaAs and GaAs-coated Si substrates. Because these films on InSb are lattice matched, they are expected to yield better overall film quality than the ones grown on GaAs and Si. This was confirmed from the comparison of X-ray FWHM of 3 $\mu$  m-thick InSb films, given in Figure 1. The film grown on InSb had X-ray FWHM of 14 arsec while those grown on GaAs and GaAs/Si exhibited FWHM of 171 and 361 arsec, respectively.

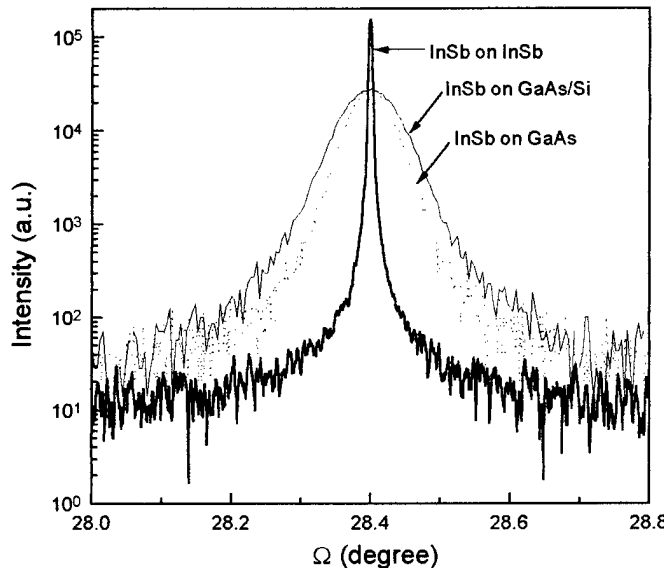


Figure 1: X-ray diffraction spectra of 3.0 $\mu$  m-thick InSb films grown on InSb, GaAs, and GaAs-coated Si substrates.

The broader peaks on GaAs and Si substrates are due to higher dislocation density. Nevertheless, these FWHM values are one of the best reported for InSb films of comparable thickness on the

respective substrates, independent of the growth technology.

For films grown on lattice mismatched substrates, the overall crystalline quality of the film is expected to depend on its thickness. Therefore, X-ray diffraction measurements were performed on InSb films of varying thickness on GaAs and Si substrates and the results are presented in Figure 2. The FWHM of InSb grown on both substrates decreases with increasing film thickness, indicating improved crystalline quality away from the highly mismatched epilayer-substrate interface.

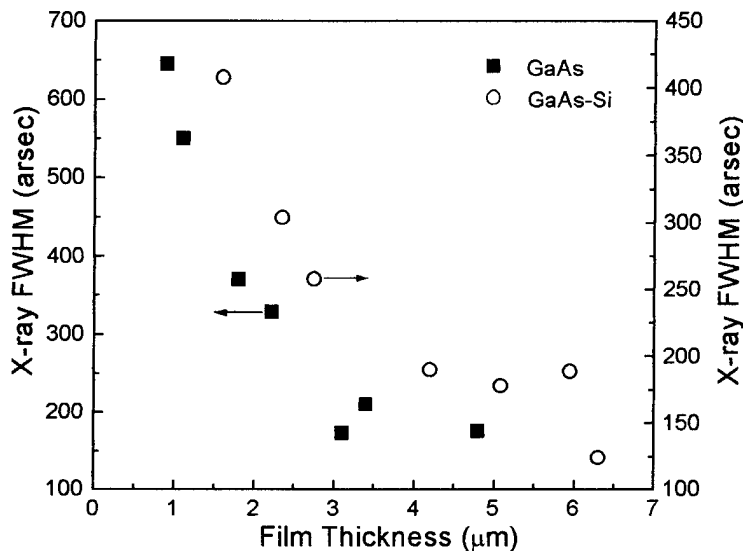


Figure 2: Dependence of the X-ray FWHM of heteroepitaxial InSb layers on film thickness.

The electrical properties of the epilayers were investigated through Hall measurements using Van der Pauw method on clover-shaped samples. The ohmic contacts are made on the samples by alloying with In-Sn at 350° C under 10% H<sub>2</sub> : 90% N<sub>2</sub> ambient. The current and magnetic field directions are separately reversed to eliminate any Hall-probe misalignment.

Figure 3 shows the room temperature Hall mobility for InSb films grown on GaAs substrates. The Hall mobility is found to improve with increasing thickness. Similar to the X-ray results, this trend reflects the decrease of dislocation density away from the interface. The Hall coefficient R<sub>H</sub> was negative and the carrier concentration of the InSb films was generally in the range of  $1 \times 10^{16} \text{ cm}^{-3}$  to  $3 \times 10^{16} \text{ cm}^{-3}$  at 300 K. The Hall coefficient remained negative at 77 K but the Hall mobility decreased dramatically far below expected values for n-type InSb. This might indicate that the as-grown layer is p-type. To identify this, more detailed analysis on this behavior has been done using the three-layer model consisting of a surface electron accumulation layer as

postulated by Soderstrom et al., an interface layer with high density of dislocations , and a bulk like layer with a highly reduced defect density. The theoretical results with the assumption of p-type InSb layer showed good agreement with the experimental observations verifying the growth of p-type InSb on GaAs substrates.

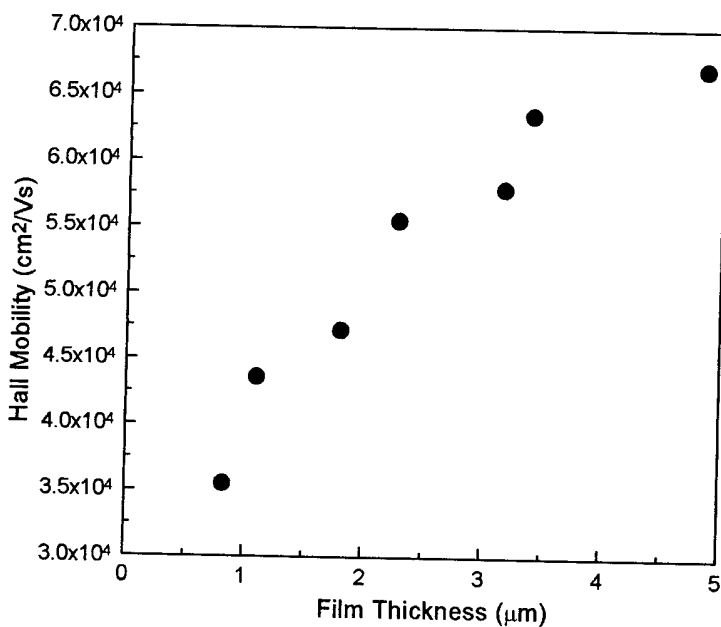


Figure 3: Variation of room temperature Hall mobility of heteroepitaxial InSb layers as a function of film thickness.

In an attempt to improve the electrical properties, a special-grade TMSb was used instead of the electronic-grade TMSb. Using the new source, InSb films with thickness ranging from  $1.2\mu\text{m}$  to  $3.6\mu\text{m}$  were grown under the identical conditions of previous growths. The structural quality determined from X-ray rocking curve was comparable and no noticeable change in the room temperature Hall mobilities were observed compared to previous samples grown with electronic-grade TMSb. The most striking differences were the low temperature electrical characteristics, as shown in Figure 4. The Hall mobility of the new InSb films remained relatively low for film thicknesses below  $2\mu\text{m}$  but it drastically improved beyond this thickness. A  $3.6\mu\text{m}$ -thick InSb films exhibited mobility of  $56,000\text{ cm}^2/\text{Vs}$  at  $300\text{ K}$  which increased to about  $80,000\text{ cm}^2/\text{Vs}$  at  $77\text{ K}$ . This temperature dependence of the Hall data differs considerably from our previous results and in fact resembles that of a n-type bulk material. The background carrier concentration at  $77\text{ K}$  was comparable to the previous InSb samples up to  $2\mu\text{m}$  in film thickness

but decreased by nearly an order of magnitude to  $10^{15} \text{ cm}^{-3}$  for thicker samples. These Hall data are comparable to the best epitaxially grown InSb results, irrespective of the growth technique.

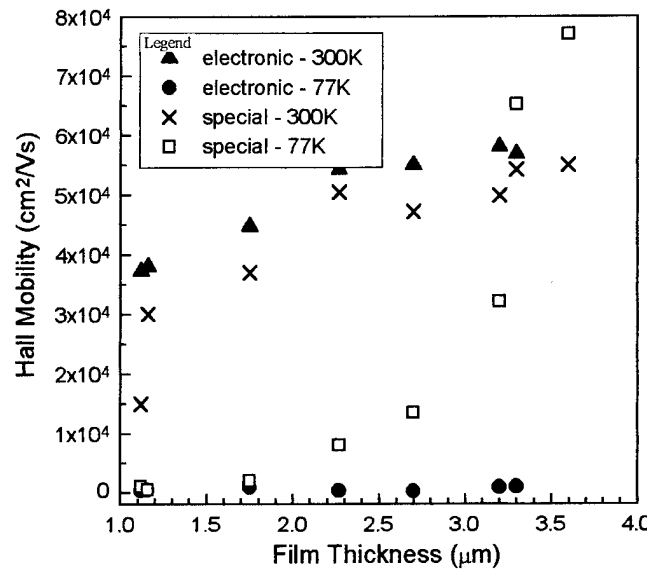


Figure 4(a): Comparison of 300K and 77K Hall mobility of undoped InSb grown using electronic- and special-grade TMSb

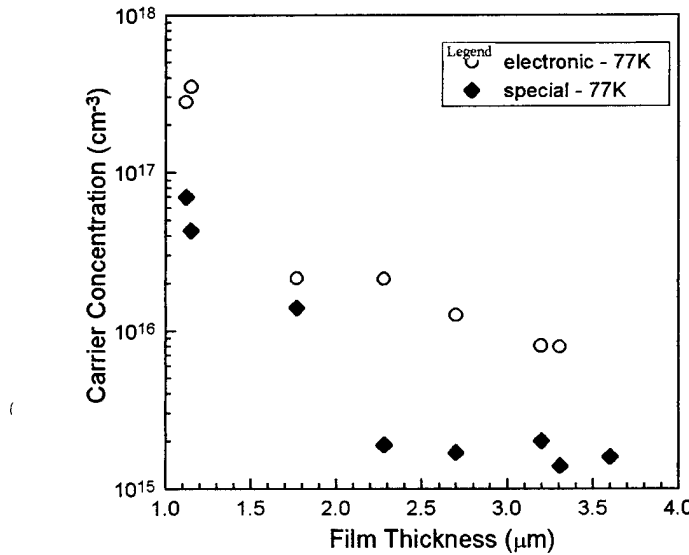


Figure 4(b): Comparison of the 77K carrier concentration of nominally undoped InSb grown using electronic- and special-grade TMSb.

Since the growth conditions and environment are identical between the previous growth with electronic-grade TMSb and the new series of growth with special-grade TMSb, the changes

in electrical properties are attributed to an absence of some impurities in the special-grade TMSb that were otherwise present in the electronic-grade TMSb. The impurities, which have not yet been identified, most likely provided a strong p-type background in the old samples. In the new samples, the background is predicted to be n-type since the Hall measurements reflected the high-mobility electron characteristics.

## 2. Demonstration of the first growth of InTlSb

Cyclopentadienylthallium (CPTl) was used as the source of thallium. CPTl is a solid with low vapor pressure at room temperature and sublimes at 120° C in vacuum (~0.1 torr). It has been previously used for growing thallium(III) oxide, a compound that has drawn interest with the discovery of high-temperature superconducting Tl-Ba-Ca-Cu oxide. Thallium flow was introduced into the growth chamber without perturbing other growth parameter settings.

This has led to the first successful growth of InTlSb. The InTlSb layer was grown on top of an InSb buffer layer. The thallium incorporation was confirmed through several independent measurements: x-ray diffraction, Auger electron spectroscopy, and optical measurements. The x-ray profile taken at (800) diffraction orientation showed resolved peaks corresponding to InSb and InTlSb (Figure 5). As compared to an InSb reference Auger spectrum, the spectrum of InTlSb exhibited an additional peak associated to thallium.

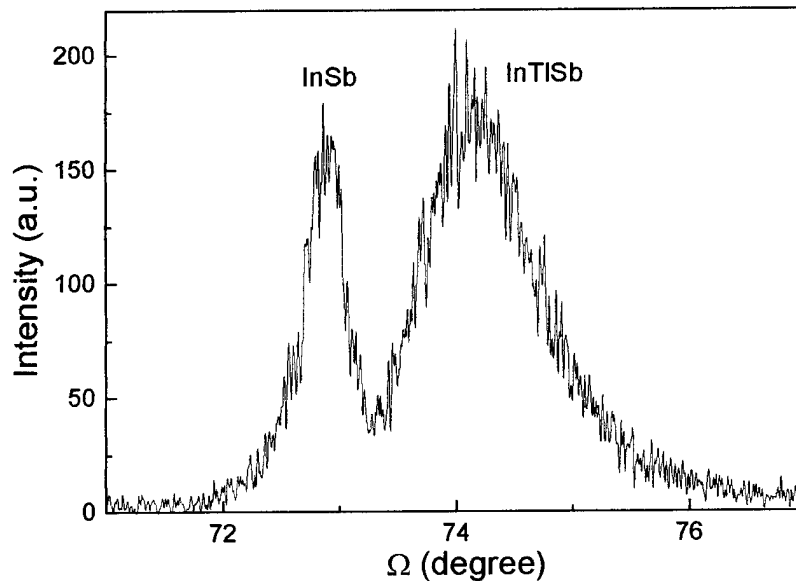


Figure 5: X-ray diffraction profile of InTlSb/InSb samples at (800) orientation.

However, the absolute composition of the alloy could not be determined since a InTlSb with known Tl concentration is not available for calibration purpose. Once the successful growth of InTlSb has been proven, Tl flow was varied to grow InTlSb alloys of different Tl composition. From the X-ray measurements, the peak corresponding to InTlSb was observed to broaden and shift away from the InSb peak as the thallium content was increased. The InSb peak remained at the same angular position. The broadening trend is clearly reflected in Figure 6 which plots the FWHM of InTlSb peak as a function of the lattice mismatch  $\Delta a/a$  between InSb and InTlSb. Both the FWHM and the mismatch were obtained directly from the X-ray profile. The broadening of the InTlSb peak has been attributed to an increase in the dislocation density arising from the increased mismatch with InSb as the thallium concentration increases.

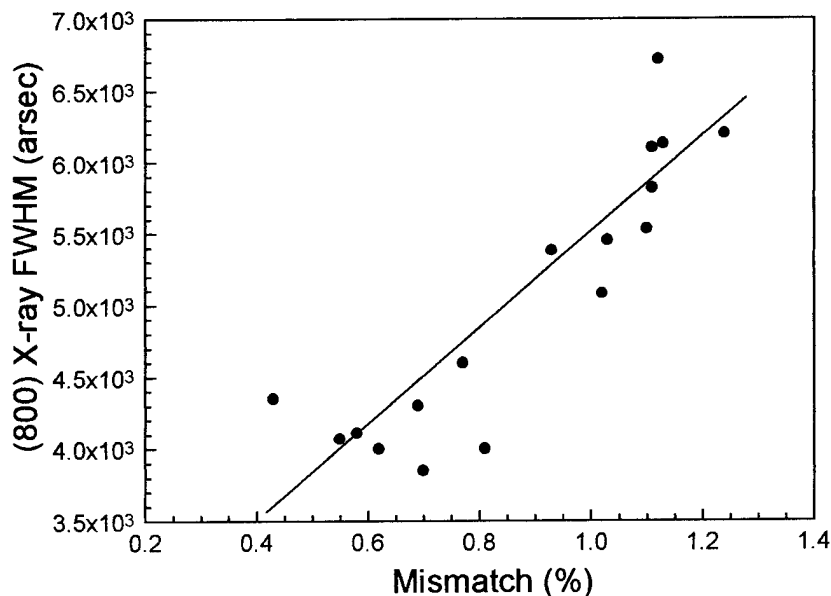


Figure 6: (800) X-ray FWHM of InTlSb layer as a function of its lattice mismatch with InSb.

Electrical characterization of InTlSb samples have shown the Hall data to be sensitive to the growth condition, in particular the thallium flow. For the range of InTlSb samples we have investigated, room temperature Hall mobility ranged from  $2 \times 10^4 \text{ cm}^2/\text{Vs}$  to  $5 \times 10^4 \text{ cm}^2/\text{Vs}$ , and an electron concentration ranging from  $1 \times 10^{16} \text{ cm}^{-3}$  to  $5 \times 10^{16} \text{ cm}^{-3}$ . Since a direct assessment of thallium is not possible at this time, the lattice mismatch between InTlSb and InSb has been used as an indirect indicator of thallium content in the material. The Hall mobility decreased monotonically with increasing thallium flow, while the electron concentration simultaneously increased. The increase in electron concentration is typical of an intrinsic semiconductor with decreasing bandgap. The decrease in mobility is attributed to an increase in alloy scattering with

increasing Tl content.

Measurements at 77 K indicate an opposite trend for the mobility and scattered data for the electron concentration. This behavior is likely to occur because of the multiple contribution of parallel conduction channels which can provide misleading conclusion to the mobility, and carrier type and concentration measured using Hall system. This can be especially true in our InTlSb samples whose non-specular surface can increase surface states and conduction. In addition, the presence of InSb buffer layer introduce an additional complexity to the analysis of the electrical data.

In order to confirm the bandgap shift, photoconductivity measurements have been performed on the InTlSb/InSb samples. The shape of the spectral response was independent of the bias applied to the photoconductor. Figure 7 shows the normalized spectral response of the InTlSb samples at 77 K. Photoresponse with an onset wavelength up to 9.5  $\mu\text{m}$  has been obtained. In general agreement with the theoretical prediction, the samples grown at higher Tl flows exhibited longer response wavelengths.

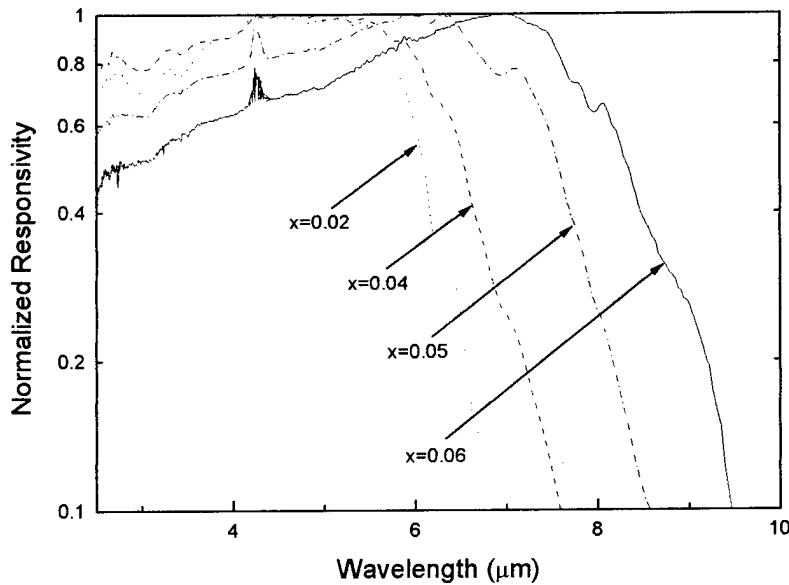


Figure 7: The normalized spectral response of the  $\text{In}_{1-x}\text{Tl}_x\text{Sb}$  photoconductors at 77 K.

The relationship of increasing photoresponse onset wavelength, and thus increasing thallium composition, to the lattice mismatch ( $\Delta a/a$ ) was evidenced in Figure 8. The cut-off wavelength has been determined as the wavelength for which the photoresponse falls at 10 % of its maximum value. A quasi-linear dependence is observed between the photoresponse cut-off wavelength and lattice mismatch, suggesting that the cut-off wavelength can be further extended with increasing

thallium content. Furthermore, a  $9.5\mu\text{m}$  cut-off wavelength corresponds to a lattice mismatch of approximately -1.3 % which is smaller than for an InAsSb alloy having a similar cut-off wavelength. This is important for the development of device-quality material with reduced dislocation density.

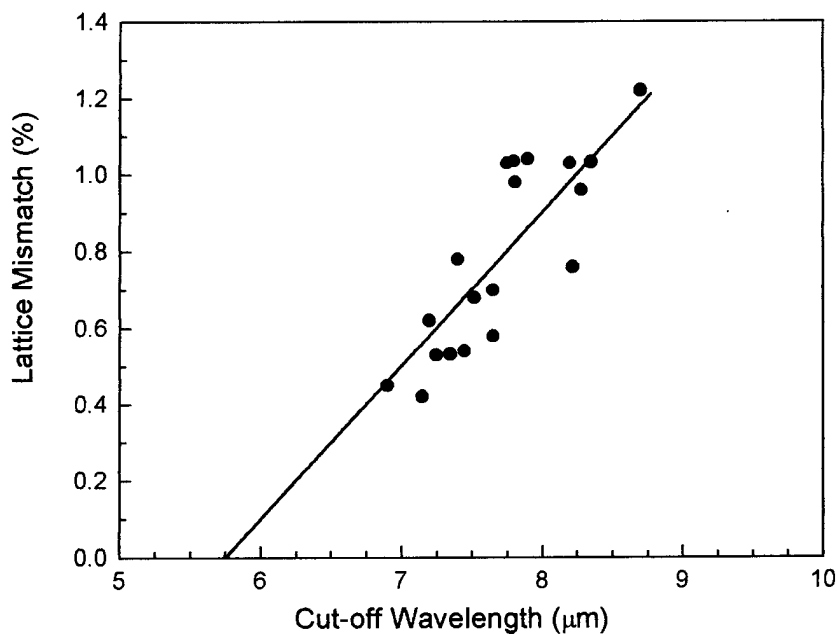


Figure 8: Dependence of the lattice mismatch between InTlSb and InSb on the 77K cut-off wavelength of InTlSb. The cut-off has been determined as the wavelength for which the photoresponse falls at 10 % of its maximum value.

### 3. Demonstration of the first growth of InTlP

As aforementioned,  $\text{TiP}_3$  has a lattice constant of  $5.94\text{\AA}$  close to that of InP ( $5.87\text{\AA}$ ) with a stable zinc blende structure. Furthermore,  $\text{TiP}_3$  is expected to be a semi-metal with energy gap of around -0.27 eV. Thus, the growth of  $(\text{InP})_{1-x}(\text{TiP}_3)_x$  by Tl incorporation into InP has been attempted as a next step to achieve long-wavelength material.

The surface morphology of both InP and  $(\text{InP})_{1-x}(\text{TiP}_3)_x$  epilayers was nearly specular, with only a few randomly scattered hillocks. X-ray diffraction measurement of  $(\text{InP})_{1-x}(\text{TiP}_3)_x/\text{InP}$  layer showed one peak at the angle corresponding to InP. This is not an unexpected result considering that the lattice-mismatch between the two crystals is small. Despite the similarities in these structural characteristics, a significant difference in the growth rate between InP and  $(\text{InP})_{1-x}(\text{TiP}_3)_x$  was found. From the measured thicknesses of the epilayers grown for 2 and 1/2 hours, the growth rate has been determined to be  $0.60\text{ }\mu\text{m/hr}$  for InP and  $0.78\text{ }\mu\text{m/hr}$  for  $(\text{InP})_{1-x}(\text{TiP}_3)_x$ . This increase in the growth rate for  $(\text{InP})_{1-x}(\text{TiP}_3)_x$  is attributed to the presence of an

additional group-III element, which usually determines the growth rate because of their high sticking coefficient under group-V rich environment.

Both InP and  $(InP)_{1-x}(TlP_3)_x$  layers exhibited excellent electrical characteristics as determined by Hall measurements. The Hall coefficient sign of the samples were negative, indicating n-type materials. Hall mobility of a 1.7  $\mu m$ -thick InP sample was as high as  $4,200 \text{ cm}^2/\text{Vs}$  at 300 K and  $73,000 \text{ cm}^2/\text{Vs}$  at 77 K while the Hall mobility of a 1.6  $\mu m$ -thick  $(InP)_{1-x}(TlP_3)_x$  sample was  $4,600 \text{ cm}^2/\text{Vs}$  at 300 K and  $77,000 \text{ cm}^2/\text{Vs}$  at 77 K. The higher mobility of  $(InP)_{1-x}(TlP_3)_x$  is indicative of a smaller electron mass for the lower bandgap material. The carrier concentration of both samples was approximately  $2 \times 10^{14} \text{ cm}^{-3}$  at 77 K and 300 K.

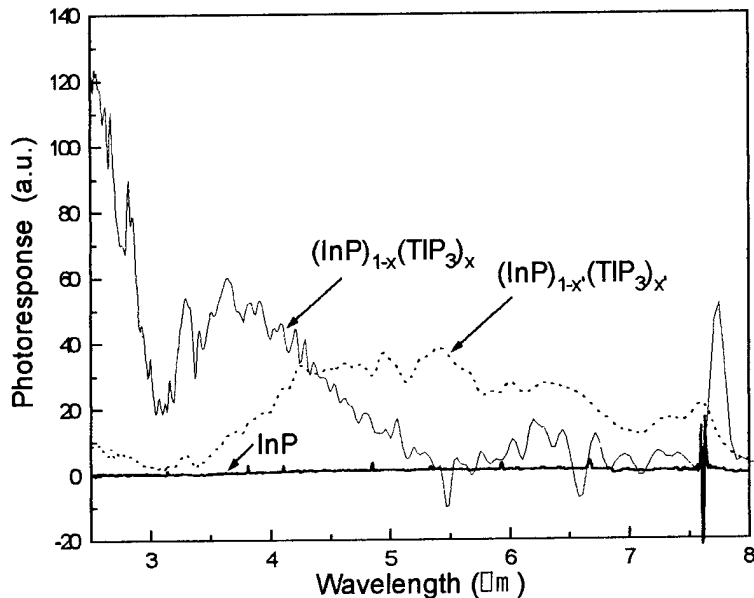


Figure 9: Photoresponse spectra of  $(InP)_{1-x}(TlP_3)_x$  with different compositions.

The most interesting results were found from infrared photoconductivity measurements. Simple photoconductors were fabricated from samples grown on semi-insulating InP substrates. Fig. 9 displays the 77 K photoconductivity spectral responses of InP and  $(InP)_{1-x}(TlP_3)_x$  samples with different x values. As anticipated, there is no spectral response from the InP sample in the infrared wavelength region. Clear photoresponse is observed from both the Tl-containing samples, with  $(InP)_{1-x}(TlP_3)_x$  having an onset wavelength around 5.5  $\mu m$  and  $(InP)_{1-x}(TlP_3)_x$ , around 8.0  $\mu m$ . This is consistent with our predicted trend since the Tl content in  $(InP)_{1-x}(TlP_3)_x$  is expected to be greater as it was grown under a higher thallium flow than  $(InP)_{1-x}(TlP_3)_x$ . Schilfgaarde et al. have calculated some physical properties of the theoretical TlP compound. They predicted TlP to exhibit a zinc blende structure with a lattice constant of 5.96  $\text{\AA}$ . This prediction closely resembles the aforementioned properties of  $TlP_3$ . Assuming the bandgap energy of  $TlP_3$  to be the same as that of TlP ( $E_g = -0.27\text{eV}$ ), a rough estimate of  $(InP)_{1-x}(TlP_3)_x$  stoichiometry can be calculated based on our optical measurements, the composition for  $(InP)_{1-x}(TlP_3)_x$  samples with onset wavelengths of 5.5  $\mu m$  and 8.0  $\mu m$  are  $x=0.6$  and 0.64, respectively.

#### **4. Demonstration of the first growth of InTlAsSb**

Even though InAsSb, InTlSb, InSbBi, InAsBi, InTlP, and InTlAs have been investigated and suggested as alternatives, further reduction of the band gap is still necessary for the high performance detector operation in the LWIR range. As an another approach, incorporation of Bi or Tl into InAsSb, InGaSb, and InGaP has been considered to reduce the band gap of the ternary alloys. In spite of the many efforts to grow InAsSbBi, InGaSbBi, and TlInGaP with advanced growth techniques such as metalorganic chemical vapor deposition (MOCVD) and molecular beam epitaxy (MBE), it is true that there has been no report on the LWIR photoresponse observation from III-V quaternary alloys until now.

Film deposition was carried out in a horizontal cold wall LP-MOCVD reactor. Trimethylindium (TMI), trimethylantimony (TMSb), cyclopentadienylthallium (CPTl), and 5 % arsine ( $\text{AsH}_3$ ) were used as precursors of indium, antimony, thallium, and arsenic, respectively. The reactor pressure was 100 mbar for all of the growth and temperature was around 455 °C. The substrates used in this study were superclean semi-insulating GaAs (001) with a typical size of  $1.0 \times 1.0 \text{ cm}^2$ .

Figure 10(a) shows the typical x-ray  $\theta$ - $2\theta$  scan profile of the InTlAsSb layer grown on GaAs substrate. There were three peaks at a range between 27° and 35°. The peaks at 28.4° and 33.0° are from the InSb buffer layer and the GaAs substrate, respectively. The remaining peak at 29.1° was assigned to the (004) diffraction from an InTlAsSb layer. The rocking curve for InTlSb grown with the same In, Tl, and Sb flow rates but without As flow was also presented [Fig. 10(b)] for comparison. It can be clearly observed that the diffraction peak is shifted toward a higher angle with the As incorporation into InTlSb, confirming the significant incorporation of As into the crystal lattice of InTlSb ternary. Typically, x-ray line width of the quaternary layer is wider than that of ternary as can be seen in Fig. 10.

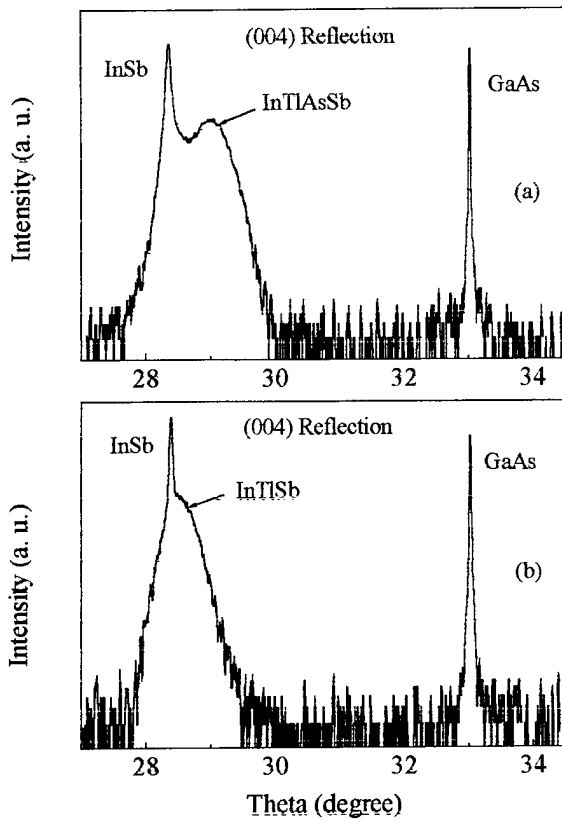


Figure 10: High resolution x-ray diffraction pattern of (a) InTlAsSb/InSb/GaAs and (b) InTlSb/InSb/GaAs. The same In, Tl, and Sb fluxes were used for the growth of InTlAsSb and InTlSb system.

In order to investigate the band gap variation due to As incorporation into InTlSb, we performed the infrared photoresponse measurements on as-grown samples using a FTIR spectrometer. Figure 11 shows the normalized spectral photoresponse of InSb, InTlSb, and InTlAsSb samples grown on GaAs substrates. Quaternary sample (b) [(d)] has the same growth conditions with ternary (a) [(c)] except for the  $\text{AsH}_3$  flux. For the InSb sample, an absorption cutoff wavelength at about  $5.5 \mu\text{m}$  was observed at 77 K, which agrees with the photoluminescence measurement. The feature around  $4.3 \mu\text{m}$  is due to the  $\text{CO}_2$  absorption in the spectrometer. A clear shift of absorption cutoff wavelength to longer wavelength up to  $8.5 \mu\text{m}$  was obtained for InTlSb [(c)], which indicates the reduction of the band gap energy of InSb by Tl incorporation. Further increase of the cutoff wavelength is achieved by incorporating As

into InTlSb alloy. A cutoff wavelength as long as  $10.8\text{ }\mu\text{m}$  is obtained from InTlAsSb [(d)] at 77 K. These results are the first observation of an infrared photoresponse at such a long wavelength from III-V quaternary alloys. The molar flow rates for sample (d) were  $3.73\text{ }\mu\text{mol/min}$  for TMI,  $0.00043\text{ }\mu\text{mol/min}$  for CPTl,  $35.74\text{ }\mu\text{mol/min}$  for TMSb, and  $9.38\text{ }\mu\text{mol/min}$  for  $\text{AsH}_3$ . A slight increase of  $\text{AsH}_3$  flow rate resulted in severe degradation of photoresponse signal, implying very narrow growth window in this material system. It is interesting to note that, as the cutoff wavelength increases, the degree of tailing in the photoresponse line becomes larger, which may be explained by the increase of band edge perturbation due to the vacancies, antisites, and other residual impurities.

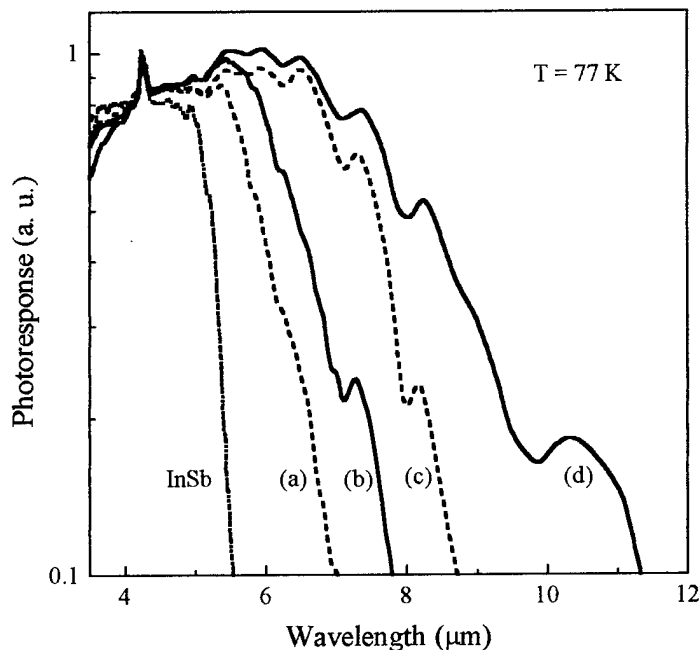


Figure 11: The normalized infrared spectral photoresponse of InSb, InTlSb, and InTlAsSb films at 77 K. Quaternary sample (b) [(d)] has the identical growth conditions with ternary (a) [(c)] except for the  $\text{AsH}_3$  flux. Note the distinct shift of cutoff wavelength to longer wavelength with the incorporation of As into InTlSb.

The InTlAsSb sample (d) with a  $10.8\text{ }\mu\text{m}$  cutoff wavelength (corresponding to a band gap of  $0.115\text{ eV}$ ) exhibited a lattice constant of  $6.4236\text{ \AA}$ , as deduced from x-ray data, which implies  $0.86\%$  lattice mismatch with InSb ( $a = 6.4794\text{ \AA}$ ). This is in striking contrast with the

implies 0.86 % lattice mismatch with InSb ( $a = 6.4794 \text{ \AA}$ ). This is in striking contrast with the InAsSb material system that has 0.175 eV band gap when the mismatch with InSb is 0.86 %. It is worthy to note that InAsSb has 2.27 % lattice mismatch with InSb when the band gap is at minimum (InAs<sub>0.35</sub>Sb<sub>0.65</sub>: 0.136 eV at 77 K). The present results thus indicate that InTlAsSb alloy can exhibit longer cutoff wavelength than InAsSb system while maintaining much less lattice mismatch with InSb. In principle, quaternary InTlAsSb alloy system has the advantages that the band gap can be tailored down to 0 eV and the lattice constant can be matched to that of InSb, which would improve the device performance by reducing the inevitable generation of misfit dislocation. A systematic study of band gap energy and lattice constant versus composition of the films is being pursued.

Figure 12 shows the spectral response of InTlAsSb sample at room temperature. LWIR photoconductivity up to 15  $\mu\text{m}$  was demonstrated for the first time. These measurements were the first observation of room temperature band edge photoresponse at such a long wavelength from III-V alloys.

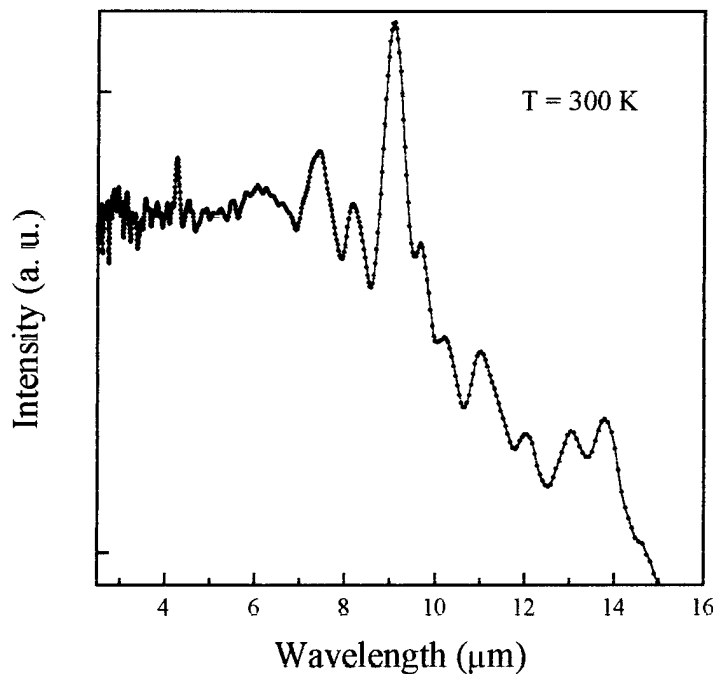


Figure 12: The spectral response of InTlAsSb sample at room temperature.

The electrical properties of InTlAsSb films with thickness of 1.4  $\mu\text{m}$  were characterized by Hall effect measurements. The Hall coefficient for the undoped samples was negative at room temperature. Figure 13 shows the decrease of room temperature mobility from 16 100 to 6 190  $\text{cm}^2/\text{Vs}$  as the As flow rate increases. The molar flow rates of TMI, CPTl, and TMSb were fixed in this study. The decrease of mobility may be due to the increase of impurity and random alloy scattering. Random alloy scattering is known to be significant in other InSb based alloy such as InAsSb. The room temperature electron concentration increased from  $8.8 \times 10^{16}$  to  $3.8 \times 10^{17} \text{ cm}^{-3}$  with the increase of As flow rate. For the InTlAsSb sample with a 10.8  $\mu\text{m}$  cutoff wavelength, the electron concentration was  $1.6 \times 10^{17}$  and  $7.6 \times 10^{16} \text{ cm}^{-3}$  at 300 and 77 K, respectively.

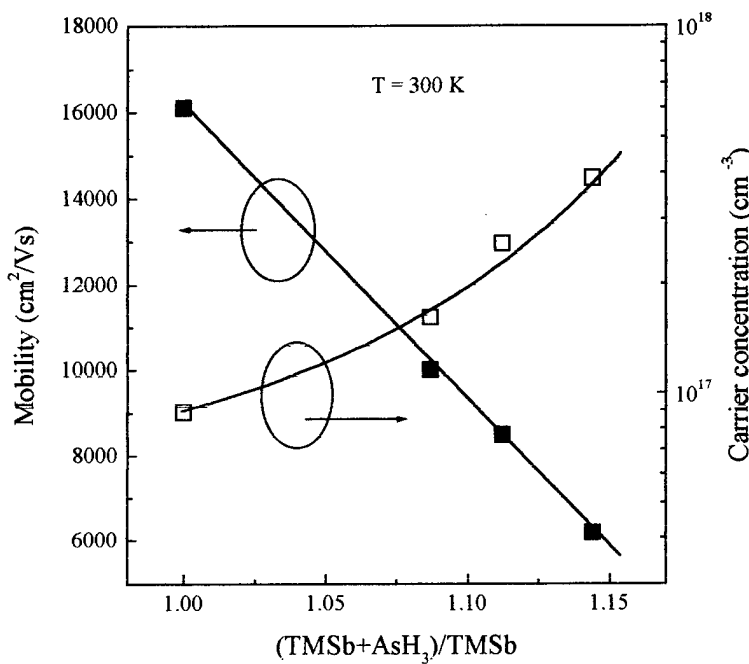


Figure 13: Room temperature mobility and carrier concentration of InTlAsSb as a function of group V gas flow rate ratio,  $(\text{TMSb} + \text{AsH}_3)/\text{TMSb}$ . The molar flow rates of TMI, CPTl, and TMSb were fixed in this study. The lines were drawn to guide the eye.

## 5. Growth of high quality InSbBi

### Growth

For the growth of InSbBi alloy, InSb buffer layer was first grown under the optimum growth conditions determined from the InSb investigations. The growth of InSbBi was then attempted by introducing a small flow of TMBi without altering other growth parameters. Once the growth of InSbBi has been verified, different amount of Bi was sent to the growth chamber in an attempt to obtain InSbBi alloy with different Bi composition. This was achieved by varying both the bubbler temperature as well as the flow rate of TMBi.

### Structural Characteristics

Figure 14 shows the x-ray diffraction pattern for an as-deposited InSbBi film on the InSb substrate at (004) reflection. Two distinct peaks around  $28.5^\circ$  were observed. The x-ray peak corresponding to the InSb substrate is observed at an angle of  $28.39^\circ$ . The x-ray peak at an angle of  $28.49^\circ$  is attributed to the InSbBi and clearly distinguishable from that of InSb substrate.

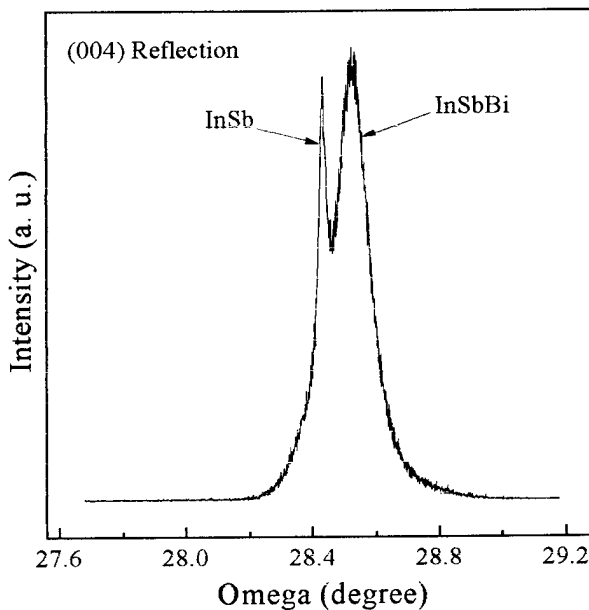


Figure 14: X-ray diffraction pattern of InSbBi/InSb epitaxial layers at (004) reflection.

### Chemical Analysis by X-ray Spectroscopy

In order to verify the incorporation of Bi into InSb, energy dispersive x-ray analysis (EDAX) measurement was performed on InSbBi sample. Figure 15 provides the EDAX spectra of an InSbBi sample along with that of an InSb. No elements were detected other than expected

In, Sb, and Bi in the spectra. Compared to the reference InSb sample, a peak corresponding to Bi (Bi M<sub>α</sub> line) is identified for the InSbBi/InSb sample, confirming the incorporation of Bi in the epitaxial layer.

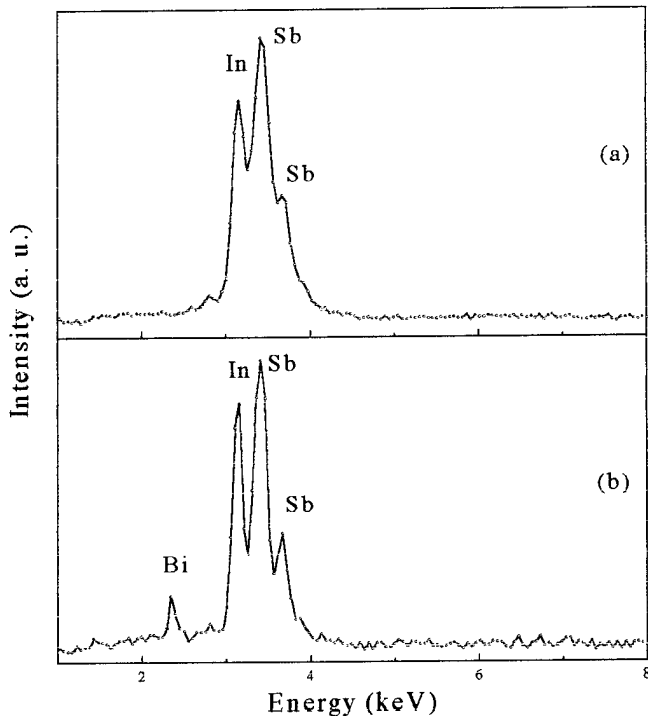


Figure 15: Energy dispersive x-ray analysis (EDAX) spectra of the (a) InSb and InSbBi/InSb layers.

### Optical Characteristics

The reduction of the band gap energy by the addition of Bi into InSb was verified through optical measurements. Optical absorption measurements were first carried out to study the effect of Bi incorporation on the band gap energy and verify the band gap energy reduction. Figure 16 shows the difference of absorption coefficients between InSb and InSbBi which is extracted from the transmission spectra. As can be seen in this figure, the difference of the absorption coefficient between the two materials is quite substantial especially in the region beyond 6  $\mu\text{m}$ . It is also clear that the incorporation of Bi in InSb shifts the absorption edge to a smaller energy. The band gap energy of investigated InSb<sub>0.96</sub>Bi<sub>0.04</sub> sample roughly estimated from the absorption coefficient of 500  $\text{cm}^{-1}$  was 0.11 eV at room temperature.

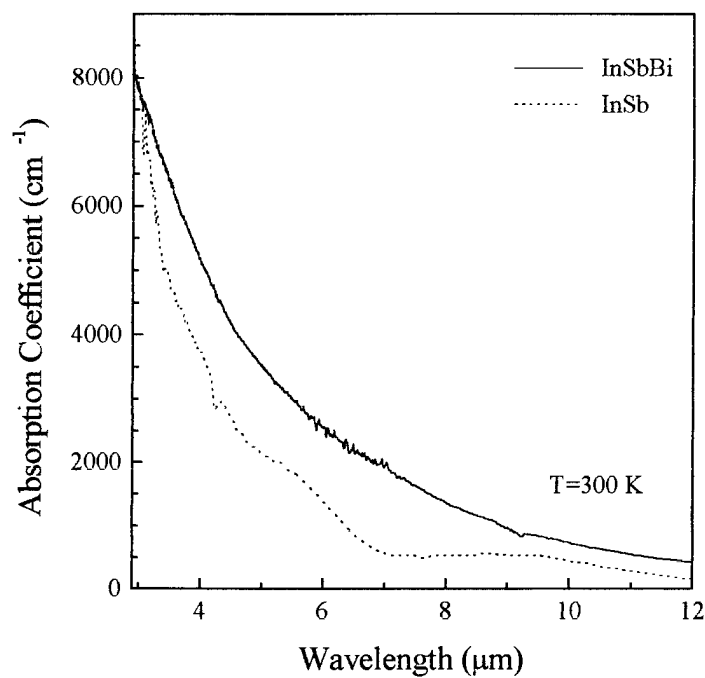


Figure 16: Absorption coefficient of InSb (dashed line) and InSbBi (solid line) as a function of wavelength at room temperature.

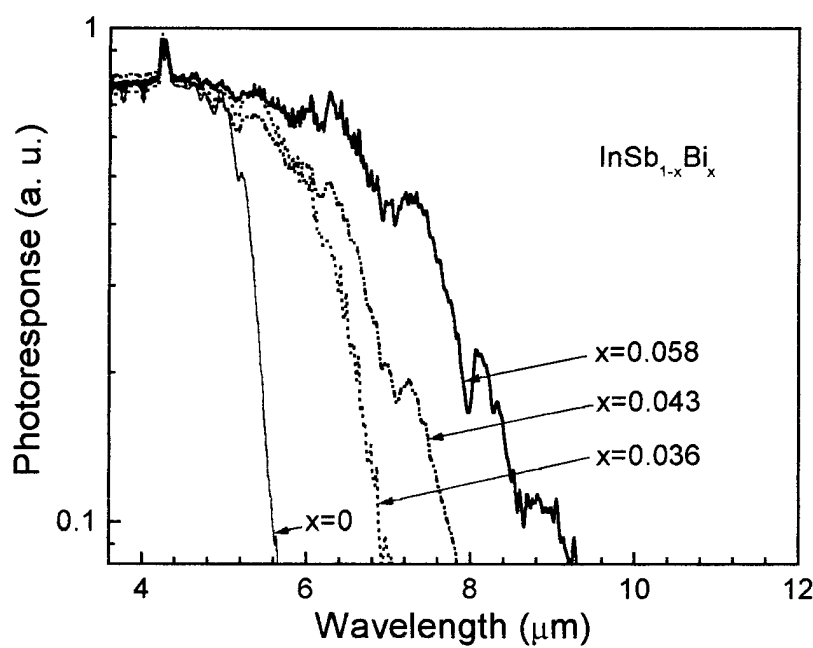


Figure 17: The normalized spectral photoresponse of InSb and InSbBi at 77 K.

Photoresponse measurements were performed on as-grown samples using FTIR spectrometer. Figure 17 shows the normalized photoresponse spectra of selected InSbBi samples along with a photoresponse of a reference InSb. A distinct shift of absorption edge from 5.5 for InSb up to 9.3  $\mu\text{m}$  for InSbBi was observed at 77 K. In general agreement with the theoretical prediction, the samples grown at higher Bi input flows exhibited longer response wavelengths. The bump around 4.3  $\mu\text{m}$  is due to the carbon dioxide absorption in the spectra.

### Electrical Characteristics

The efficiency and reliability of optical devices such as photodetectors and semiconductor lasers are affected critically by type and concentration of autodoped impurities. In this section, electrical characteristics were investigated in the InSbBi epitaxial films. The electrical properties of InSbBi films with thickness varying between 1.4-2.0  $\mu\text{m}$  were characterized by Hall measurements. At both 77 K and 300 K, an n-type conductivity has been observed by the incorporation of Bi which is believed to substitute for Sb in the InSb lattice.

Figure 18 shows the decrease of room temperature mobility from 44,100 down to 4,910  $\text{cm}^2/\text{V s}$  as the Bi concentration increases. At 77 K, the mobility decreases from 11,000 to 1,200  $\text{cm}^2/\text{V s}$  as the Bi concentration increases. The decrease of mobility is probably due to the increase of random alloy scattering potential, which has been shown to be significant in other InSb-based compound such as InAsSb ternary alloy.

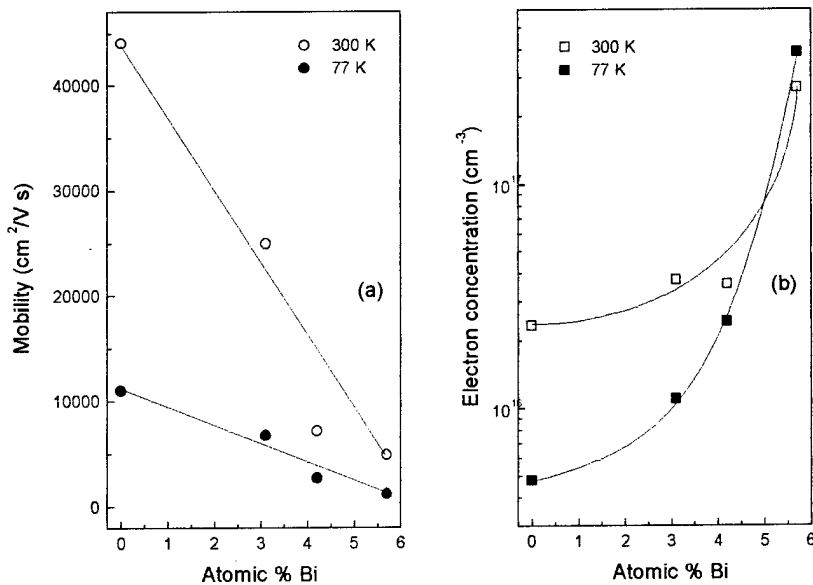


Figure 18: (a) Mobility and (b) electron concentration of InSbBi as a function of Bi content at 77 and 300 K.

As illustrated in Figure 18, the electron concentration increased from  $3.7 \times 10^{16}$  up to  $2.7 \times 10^{17} / \text{cm}^3$  with the increase of Bi incorporation at 300 K. At 77 K, the electron concentration increases from  $4.8 \times 10^{15}$  to  $3.9 \times 10^{17} / \text{cm}^3$  as the Bi concentration increases. The increase of electron concentration with the increase of Bi concentration is compatible with the decrease of energy band gap in InSbBi ternary alloys.

It can be noted that for InSbBi layer with 5.8 % Bi, the carrier concentration was higher at 77 K than at 300 K. At high temperature, the InSbBi behaves like an intrinsic semiconductor with the equal number of electrons and holes. In this region, the more mobile intrinsic electrons dominate the conductivity and determine Hall coefficient,  $R_H$ , sign. As temperature goes down, the intrinsic carriers are frozen out and the extrinsic carriers starts to dominate the conductivity in the semiconductor. If the sample is doped with acceptors, the sign of  $R_H$  will be changed from negative to positive as the temperature is lowered. It can be noticed from Fig. 18 that InSbBi with 5.8 % Bi is near the edge of carrier type conversion point at 77 K, which results in an anomalous high carrier concentration. This implies that the grown InSbBi sample was unintentionally doped with acceptors and would show p-type behavior at low temperature, somewhere below the studied temperature. The anomalous behavior in Hall measurements has been reported in other p-type narrow band gap materials such as InSb and HgCdTe.

## Task 2 InTlSb Doping and Contact

### 6. Doping of InSb, InAsSb and InTlSb

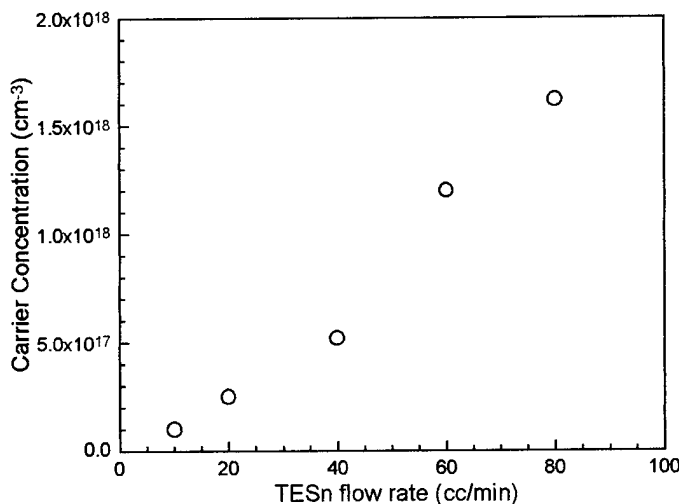


Figure 19: N-type doping concentration dependence on TESn flow rate.

Following the work of Biefeld et al., tetraethyltin (TESn) was used as an n-type dopant source. The TESn was kept at a temperature of -25° C and the flow rate was varied from 7 cc/min to 80 cc/min, resulting in doping levels ranging from  $5 \times 10^{16} \text{ cm}^{-3}$  to  $1.2 \times 10^{18} \text{ cm}^{-3}$  (Fig. 19). No degradation in surface morphology and x-ray FWHM were observed. Furthermore, we did not notice any memory effect associated with TESn, consistent with the reported work. In order to access the activation energy of Sn dopant in InSb, the carrier concentration (log scale) as a function of temperature has been plotted. Using the relation that the ionized carrier concentration is proportional to  $\exp(-E_i/kT)$ , where  $E_i$  is the activation energy,  $k$  is the Boltzmann's constant and  $T$  is the temperature,  $E_i$  has roughly been estimated to be a few tenth of meV.

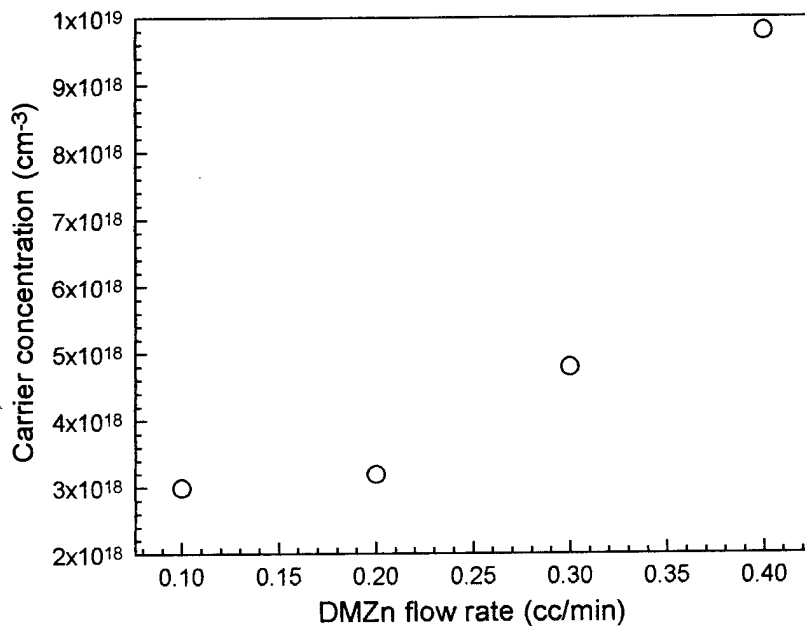


Figure 20: P-type doping concentration as a function of DMZn flow rate.

P-type doping of InSb was first carried out using dimethylzinc (DMZn). Its bubbler was maintained at a constant temperature at -25° C. The zinc flow was diluted after passing through the bubbler. The dilution flow was kept at 1200 cc/min. Using a 100 cc/min capacity mass flow controller, only concentrations greater than  $8 \times 10^{18} \text{ cm}^{-3}$  were obtained. In order to have a better flow rate control, a smaller capacity mass flow controller (10cc/min) was installed. This enabled us to lower the doping concentration to approximately  $3 \times 10^{18} \text{ cm}^{-3}$  (Fig. 20).

To further extend our doping ranges to lower levels, diethylzinc (DEZn) has been

purchased to replace DMZn. DEZn has a much lower vapor pressure than DMZn and is the preferred zinc source for p-type doping of III-V epitaxial alloys. The DEZn bubbler has been kept at 10° C and the flow was varied from 0.1 cc/min to 0.45 cc/min. The corresponding doping level from  $8.26 \times 10^{16} \text{ cm}^{-3}$  to  $1.31 \times 10^{18} \text{ cm}^{-3}$  has been achieved (Fig. 21). Even lower doping level of  $3.06 \times 10^{16} \text{ cm}^{-3}$  has been achieved by lowering the DEZn bubbler temperature down to -15°C and flowing 0.20 cc/min hydrogen. From the log plot of carrier concentration as a function of temperature, the activation energy of Zn in InSb has been estimated to be a few meV.

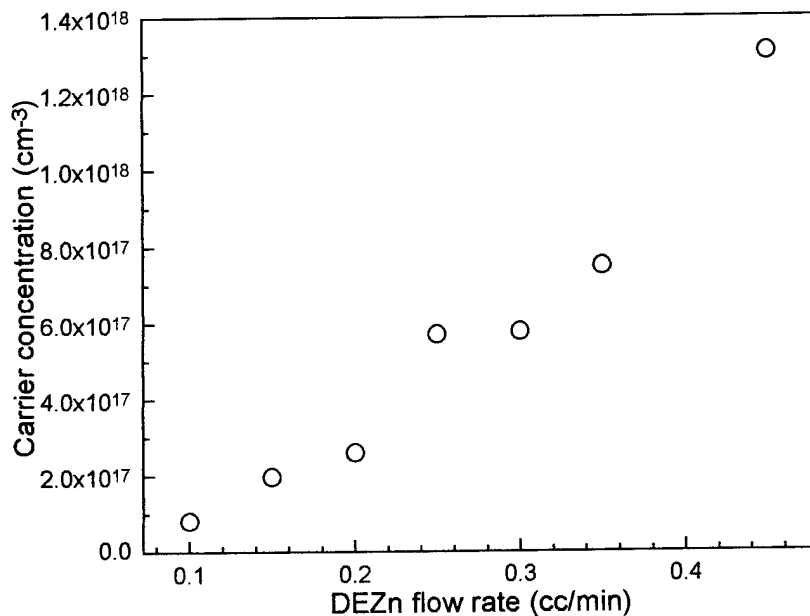


Figure 21: P-type doping concentration as a function of DEZn flow rate.

Once the doping of InSb has been realized, doping of InAsSb and InTlSb epitaxial films has been attempted using the same dopant sources. Even though no systematic studies on the doping of these alloys have been performed, several experimental results showed the similar doping characteristics for InSb, InAsSb and InTlSb using Sn and Zn.

## 7. Development of Device Processing Technology

### Etching

The first step in fabrication of photodetector is to etch the mesa structure. It was performed using photolithography and wet chemical etching techniques. The mesa size has been determined to be  $400\mu \text{m} \times 400\mu \text{m}$  including the  $100\mu \text{m} \times 100\mu \text{m}$  contact area. The Shipley 1813 photoresistance has been used for the photolithography process. The etching rate and mesa

height has been measured by alpha step machine (Tencor). After prebake at 90 °C the wafer has been exposed to UV light (Kark-Suss) for 12 seconds and developed by Shipley Developer 351 for about 1 min. The post-bake was done at 120 °C for 30 min. The etching solutions were lactic:nitric acid and it was etched at room temperature.

### Metallization

Metallization was realized by an e-beam evaporator. After several trial, the metallization step has been determined. Ti/Au contact has been suggested because Ti is strongly adhesive to the semiconductor surfaces and chemically stable. It formed good ohmic contact to both n-and p-type materials. The photolithography technique was employed to get the contact pattern. The etching solutions for Au (KI:I<sub>2</sub>:H<sub>2</sub>O) and Ti (HF) are selective. Furthermore, the etching solutions for Ti (HF) and InSb (lactic:nitric) are also selective. Thus, it provides us a good way to protect the surface of InSb when the contact pattern is made by chemical etching.

### Wire bonding and mounting

The fabricated chips are mounted on the copper heat sink coated with In at a temperature of 160 °C in an ambient gas of 90 % N<sub>2</sub> and 10 % H<sub>2</sub> for 2 min. Au ball bonding has been done by Au ball bonding machine. Since InSb is mechanically soft, special care had to be taken by adjusting the force, power, time temperature during the bonding. More effort will be given to the improvement of bonding technology because the InTlSb is softer and Ti is less adhesive to this material than InSb.

## **Task 3 Fabrication of Detectors**

### **8. InTlSb photoconductors on GaAs**

The photoconductors were rectangular shaped with dimension of 3×3 mm<sup>2</sup>. Ti/Au were evaporated by an electron-beam evaporator to make ohmic contacts. Ti exhibits strong mechanical adhesion with semiconductor materials. The resistance was about 50 ohms at room temperature and increased up to several thousand ohms at 77 K. The spectral photoresponse was measured by a FTIR spectrometer with a low-noise preamplifier (Ithaco 120). The responsivity was calibrated by a blackbody test set-up, including a blackbody source, preamplifier, and chopper system. The blackbody temperature was set at 800 K. The modulating frequency was set at 400 Hz since response measurements as a function of chopper frequency showed that the thermal effect could be neglected at frequencies higher than 200 Hz.

Figure 7 in the previous section shows the spectral response of  $\text{In}_{1-x}\text{Tl}_x\text{Sb}$  (with estimated  $0.02 \leq x \leq 0.06$ ) photodetectors at 77 K, which is normalized to the peak responsivity. The cut-off wavelengths are clearly seen in the  $\text{In}_{1-x}\text{Tl}_x\text{Sb}$  photodetectors, which extend to long wavelengths with increasing Tl content. The absolute responsivity for an  $\text{In}_{0.04}\text{Tl}_{0.06}\text{Sb}$  photodetector is displayed in Fig. 22. The cut-off wavelength extends up to  $11\mu\text{m}$  at 300 K. The maximum responsivity in an  $\text{In}_{0.065}\text{Tl}_{0.035}\text{Sb}$  photodetector is about  $6.64 \text{ V/W}$  at 77 K. The corresponding Johnson-noise limited detectivity is  $7.64 \times 10^8 \text{ cm}\cdot\text{Hz}^{1/2}/\text{W}$ . The voltage responsivity and detectivity of  $\text{In}_{1-x}\text{Tl}_x\text{Sb}$  photodetectors are listed in Table II.

Table II: The performance of the  $\text{In}_{1-x}\text{Tl}_x\text{Sb}$  photoconductors at 77 K.

$\text{In}_{1-x}\text{Tl}_x\text{Sb}$ detectors	$\lambda_{\text{cut-off}}$ ( $\mu\text{m}$ )	$R_v^{\max}$ (V/W)	$D^*_{\max}$ ( $\text{cm}\cdot\text{Hz}^{1/2}/\text{W}$ )	$\mu$ ( $\text{cm}^2/\text{V}\cdot\text{s}$ )	$\tau$ (ns)
x=0.02	6.5	2.73	$2.47 \times 10^8$	$1.29 \times 10^3$	19.2
x=0.04	7.3	6.64	$7.64 \times 10^8$	$2.00 \times 10^3$	50.1
x=0.05	8.4	3.56	$8.54 \times 10^8$	$2.75 \times 10^3$	40.4
x=0.06	9.4	0.79	$2.63 \times 10^8$	$4.13 \times 10^3$	10.3

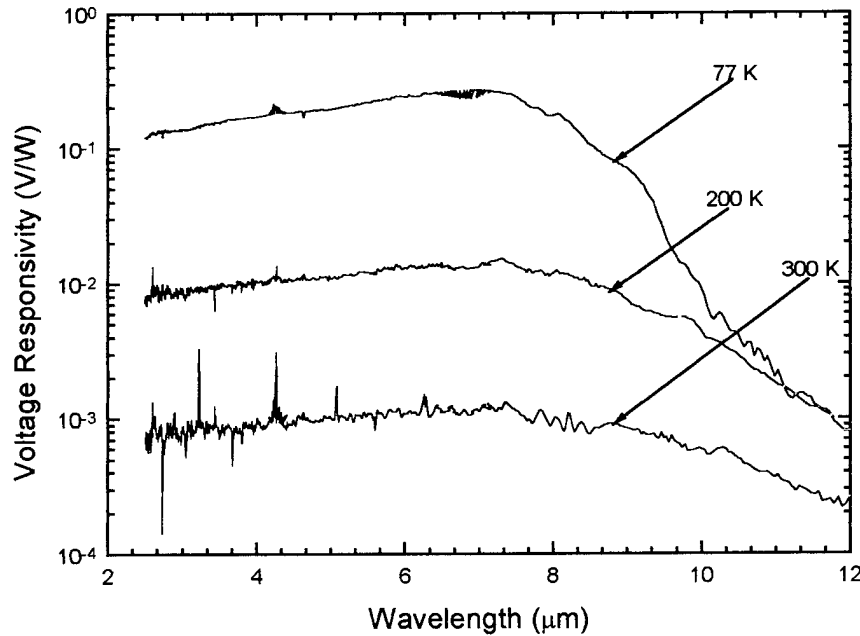


Figure 22: The spectral responsivity of  $\text{In}_{0.04}\text{Tl}_{0.06}\text{Sb}$  photoconductor at 77 K, 200 K, and 300 K.

In order to get the carrier lifetime  $\tau$ , the voltage-dependent responsivity was measured. Figure 23 shows the voltage-dependent responsivity of InTlSb photodetectors. It increases with voltage, saturates at a given voltage, and finally decreases. The saturation responsivity at large voltage can be explained by the sweep-out effect. Based on the voltage-dependent responsivity,  $\tau$  can be derived according to the simple theory of photoconductivity. The voltage responsivity can be expressed as

$$R_V = \frac{q\lambda}{hc} \frac{\eta \mu_e \tau V_b R_D}{L^2} \left(1 + \frac{1}{b}\right) \quad (1)$$

where  $q$  is the electron charge,  $\lambda$  is the incident wavelength,  $\mu_e$  is electron mobility,  $\eta$  is the quantum efficiency,  $b$  is the ratio of the electron-to-hole mobility,  $L$  is the detector length,  $V_b$  is the bias voltage, and  $R_D$  is the detector resistance. The quantum efficiency  $\eta$  can be obtained by

$$\eta = (1 - r) \frac{(1 - e^{-\alpha t})}{(1 - re^{-\alpha t})} \quad (2)$$

where  $r$  is the reflectivity,  $\alpha$  is the absorption coefficient, and  $t$  is the detector thickness. The quantum efficiency is estimated to be 64 %.

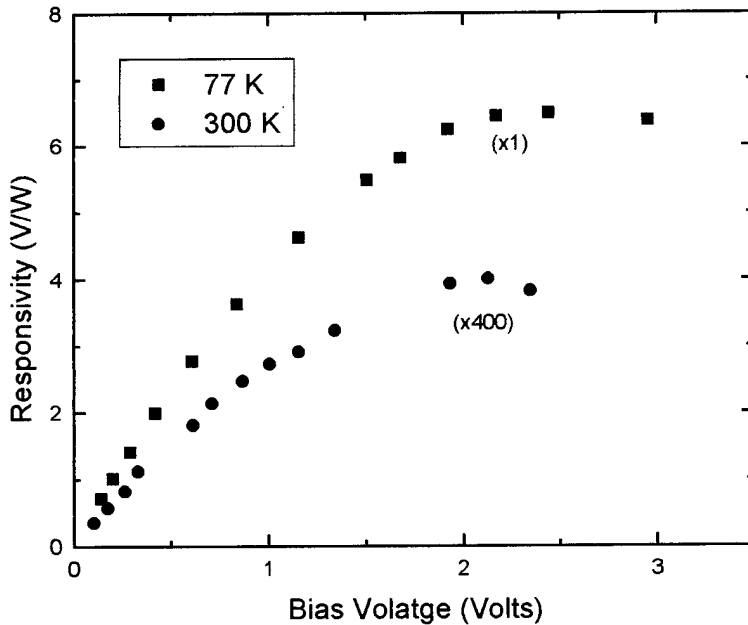


Figure 23: The voltage-dependent responsivity of an  $\text{In}_{0.06}\text{Tl}_{0.04}\text{Sb}$  photoconductor.

The effective lifetime  $\tau$  in InTlSb epitaxial layers is listed in Table II, which is 10-50 ns at 77 K. At 300 K,  $D^*$  is  $10^6$ - $10^7$  cm $\cdot$ Hz $^{1/2}$ /W and  $\tau$  is 0.1-0.6 ns.

## 9. InAsSb photoconductors on GaAs

The InAsSb photoconductor structure composes of two epitaxial layers (p-InAs<sub>0.23</sub>Sb<sub>0.77</sub> /p-InSb) grown on GaAs. The structure consisted of a 1.2 $\mu$ m InSb buffer layer and a 2.8 $\mu$ m InAs<sub>0.23</sub>Sb<sub>0.77</sub> active layer. The epitaxial layers have been grown on (100) semi-insulating GaAs substrates by LP-MOCVD at a growth temperature around 470°C. Trimethylindium (TMIn), trimethylantimony (TMSb), and 5% arsine in hydrogen are used as the precursors. P-type doping of the layer was achieved by Zn using diethylzinc (DEZn).

Structural characterization was performed using high-resolution x-ray diffraction at (400) orientation. The InSb and InAs<sub>1-x</sub>Sb<sub>x</sub> peaks were clearly resolved with a low FWHM ( $\approx$ 300 arcsec for InAsSb) indicating the high quality of the material. The composition  $x=0.77$  in the InAs<sub>1-x</sub>Sb<sub>x</sub> layer, which corresponds to the room temperature band gap of 0.12 eV, has been determined using x-ray diffraction data and Vegard's law.

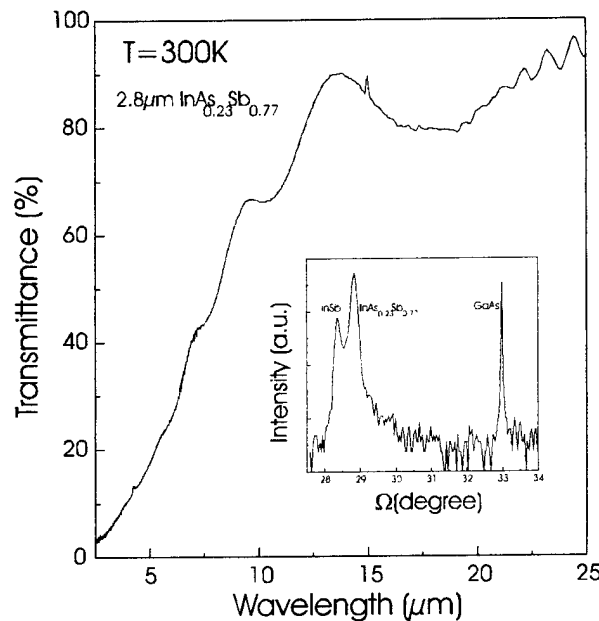


Figure 24. Room temperature infrared transmittance and X-ray diffraction spectra of InAsSb/InSb/ GaAs structure.

Hall measurements were performed on clover-patterned samples with In contacts using the van der Pauw method at both 300 K and 77 K. Hall data exhibit p-type conduction with hole concentration of  $\approx 3.6 \cdot 10^{16} \text{ cm}^{-3}$  and hole mobility of  $923 \text{ cm}^2/\text{Vs}$  at 77 K. However, it shows n-type with electron concentration of  $3 \cdot 10^{16} \text{ cm}^{-3}$  and electron mobility of  $36,000 \text{ cm}^2/\text{Vs}$  at 300 K. Infrared transmittance measurements were performed using a FTIR spectrometer at 300 K. Significant absorption at wavelengths exceeding  $10\mu\text{m}$  is clearly seen.

The geometry of the photoconductor is  $4 \times 3 \text{ mm}^2$ . Au/Ti contacts were deposited by an e-beam evaporator. The resistance is  $23 \Omega$  at 300K and  $220 \Omega$  at 200 K. Responsivity measurements as a function of chopper frequency showed that the thermal effect could be neglected at frequencies higher than 200 Hz. Figure 25 shows the spectral responsivities of a photoconductor sample at 200 K and 300 K. The peak responsivity is about  $4 \text{ mV/W}$  at  $8\mu\text{m}$  and at 300 K for 1 V bias. The cut-off wavelength around  $14\mu\text{m}$  was observed at 300 K.

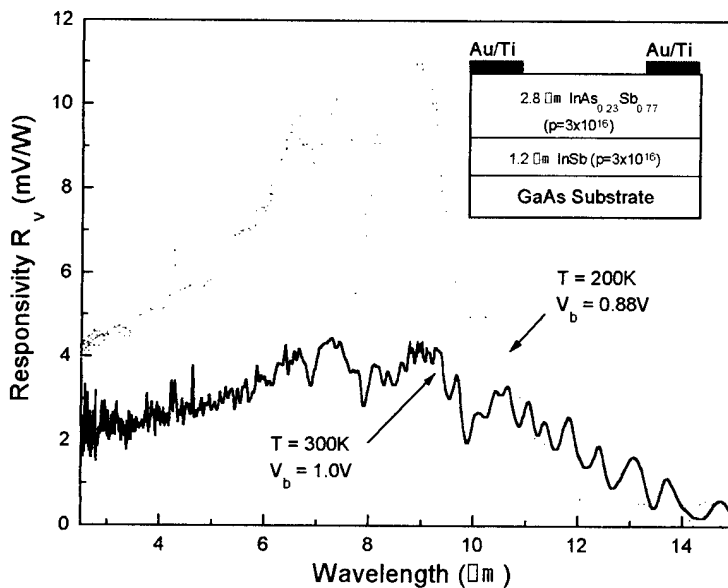


Figure 25. Spectral response of the  $\text{InAs}_{0.23}\text{Sb}_{0.77}$  photoconductor at 200 K and 300 K.

Figure 26 displays the voltage-dependent responsivity at  $10.6\mu\text{m}$ . It increases with applied-voltage and reaches saturation at around 3 volts, which corresponds to the value of  $5.8 \text{ mV/W}$  at

300 K and 10.8 mV/W at 200 K, respectively. The corresponding Johnson-noise limited detectivity of the photoconductor was then estimated to be  $\approx 3.27 \cdot 10^7$  cm·Hz<sup>1/2</sup>/W at 300 K.

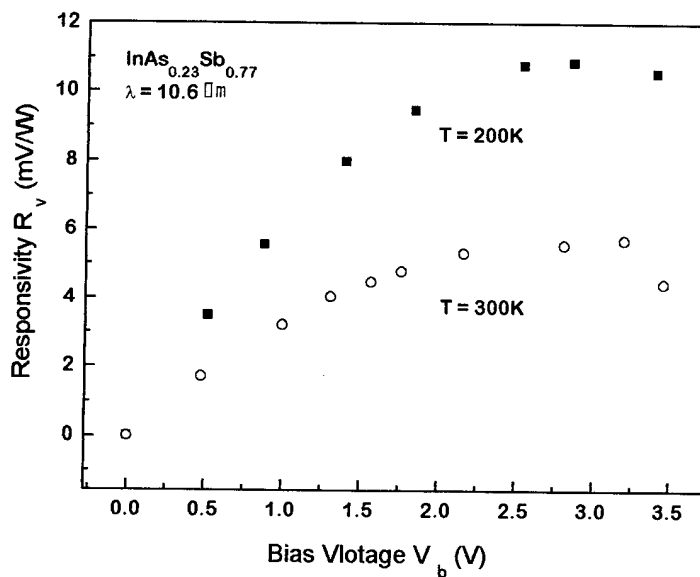


Figure 26. Voltage-dependent responsivity of the  $\text{InAs}_{0.23}\text{Sb}_{0.77}$  photoconductor at  $10.6\mu\text{m}$ .

Based on the spectral voltage-responsivity, the  $\mu_e\tau$  product and the effective lifetime  $\tau$  can be derived. Based on the electron mobility at 300 K, the effective lifetime is estimated to be 0.14 ns. The mobility-lifetime product ( $\mu_e\tau$ ) at low temperatures is lower than the room temperature value. The possible reasons for low  $\mu_e\tau$  are non-fundamental recombination mechanisms, such as Shockley-Read-Hall, surface or interface recombination. We estimated the diffusion limited mobility-lifetime product. The time necessary for the electron to diffuse through the layer to the InAsSb/InSb interface is  $\tau_D = t^2/2D_e$  where  $D_e$  is the electron diffusion coefficient and  $t$  is the layer thickness. Using the Einstein relation,  $D_e = kT\mu_e/q$ , we can calculate  $\mu_e\tau_D$ . At 200 K, the  $\mu_e\tau_D$  value was  $\approx 1.12 \cdot 10^{-6}$  cm<sup>2</sup>/V·s for a  $2.8\mu\text{m}$  thick InAsSb layer. It is comparable to the measured experimental value ( $1.13 \cdot 10^{-6}$  cm<sup>2</sup>/V·s). This indicates that the effective lifetime at low temperatures is diffusion limited and controlled by recombination occurring at the InAsSb/InSb interface. Hence, further improvements on the heterointerface is necessary for detector operation at low temperatures.

## 10. InSbBi photoconductors on GaAs

The preliminary LWIR InSbBi photoconductors were fabricated from the samples grown on semi-insulating GaAs substrates. 500 Å Au and 3000 Å Ti are evaporated by an electron beam evaporator for the ohmic contacts. The contact pattern is made using a metal mask, which covers parts of the surface during the evaporation. The active area of the photodetector was 4 mm<sup>2</sup> with a 2 mm electrode spacing. The photodetectors were mounted onto copper heat sinks and the electrical contact was made by an Au-wire bonding. The resistance of an InSb<sub>0.96</sub>Bi<sub>0.04</sub> photodetector was 435 Ω at 77 K and 110 Ω at 300 K.

The spectral response of the photodetector fabricated from the grown InSb<sub>0.96</sub>Bi<sub>0.04</sub> sample was shown in Fig. 27 for several different temperatures. The photoresponse cutoff wavelength shifts to 7.7 μm at 77 K and to 9.3 μm at 200 K. One can notice that the responsivity decreases with the increasing temperature. The signal-to-noise (S/N) ratio was too weak for adequate measurements at temperatures over 200 K.

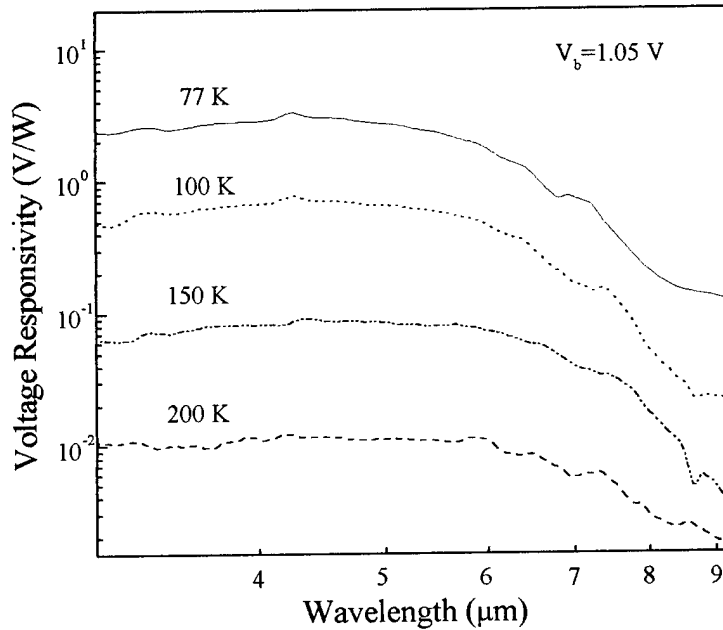


Figure 27: Spectral voltage responsivity of the InSbBi photoconductor at different temperatures.

This decrease of responsivity and S/N ratio is due to the increase of intrinsic carriers caused by the decrease of the band gap. The maximum responsivity at  $7\text{ }\mu\text{m}$  is about  $3.2\text{ V/W}$  at  $77\text{ K}$  (see Fig. 28). The corresponding Johnson-noise limited detectivity is about  $4.7 \times 10^8\text{ cm Hz}^{1/2}/\text{W}$ .

The carrier lifetime of the fabricated LWIR detector is estimated from the voltage-dependent responsivity measurements shown in Fig. 28. The measured responsivity increases linearly with the bias at low bias voltage as Eq.(1) predicts. We, however, can observe that the responsivity begins to saturate at a bias voltage of  $5.5\text{ V}$ . This saturation of responsivity can be explained by the minority carrier sweep-out at the electrode at high bias field. Taking the absorption quantum efficiency as  $\eta=0.21$  from infrared transmission measurements, the carrier lifetime-mobility product calculated from the slope of the linear portion of Fig. 28 is found to be  $\tau\mu_e=2.35 \times 10^{-4}\text{ cm}^2/\text{V}$ . Thus the carrier lifetime in InSbBi photodetector is estimated to be about  $86\text{ ns}$  at  $77\text{ K}$ . Further improvements of material quality and optimization of the structure would increase the detector performance.

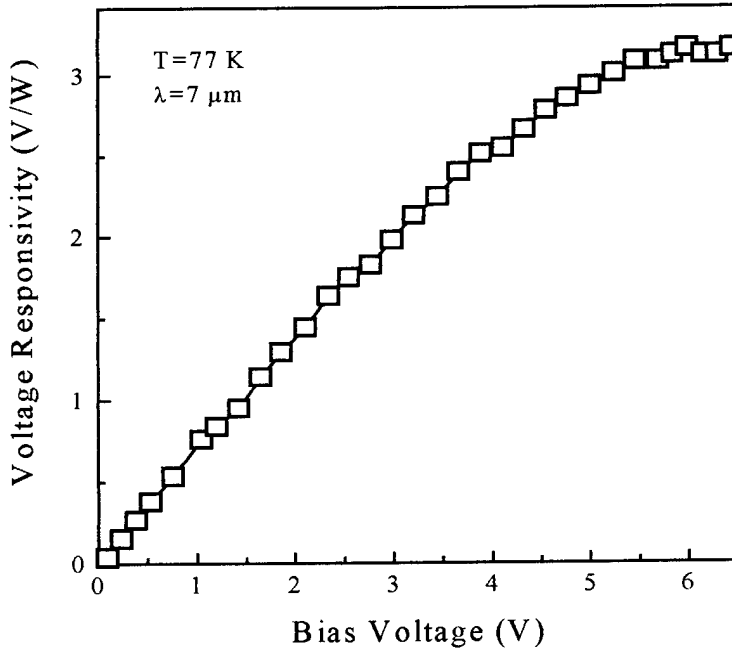


Figure 28: The bias voltage-dependent responsivity of the InSbBi photodetector at  $77\text{ K}$ .

We also have fabricated and characterized room temperature operating photoconductors

based on n-type  $\text{InSb}_{0.95}\text{Bi}_{0.05}$  for the first time. Figure 29 shows the spectral response of an  $\text{InSb}_{0.95}\text{Bi}_{0.05}$  photoconductor. The cutoff wavelength extends up to 12  $\mu\text{m}$  at 300 K. The maximum responsivity in an  $\text{InSb}_{0.95}\text{Bi}_{0.05}$  photodetector is  $7.0 \times 10^{-3}$  V/W and the corresponding Johnson-noise limited detectivity is  $4.1 \times 10^6$   $\text{cmHz}^{1/2}/\text{W}$ .

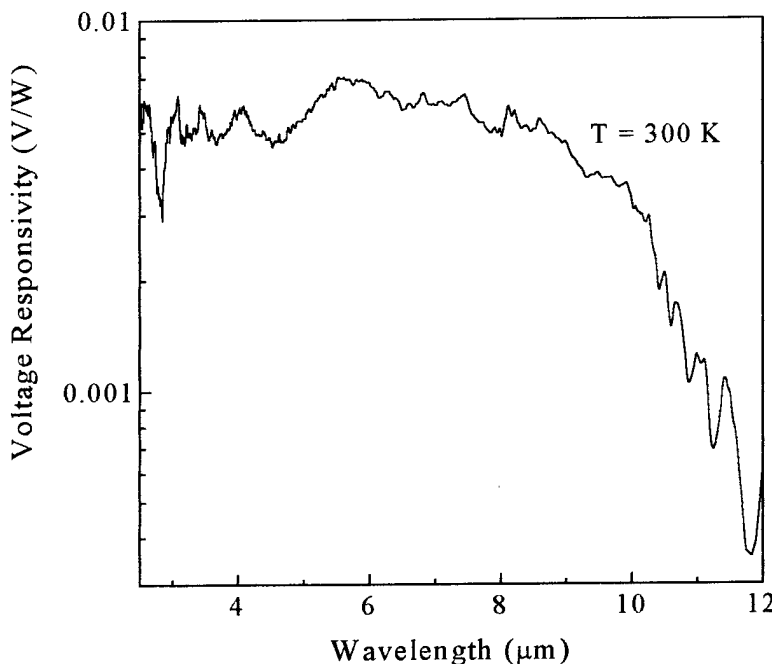


Figure 29: Spectral voltage responsivity of an  $\text{InSb}_{0.95}\text{Bi}_{0.05}$  photoconductor at room temperature.

The effective carrier life time was estimated to be about 17 ns at 300 K from the bias dependent responsivity measurements.

## 11. Photovoltaic detector Performance Measurement

For the focal plane array applications, photovoltaic devices are necessary because it requires no bias which results in the reduced thermal heating. To develop the technical line for the future InTISb photodiode applications, well established materials such as InSb and InAsSb photodiode have been fabricated using device processing step described above. The performance of the photodiode has also been measured.

### Photodiode measurement set up

The current voltage characteristics has been measured by Hewlett Packard I-V tracer. In order to analyze the dark current mechanisms in the devices, temperature dependent  $R_0A$  product has also been measured within a small current of  $\mu\text{A}$  order between 77 K and 300 K. The spectral response measurement were carried out by a Mattson FTIR spectrometer. Absolute responsivity has been obtained using the blackbody test set up described in the section 1 of this report.

### InSb photovoltaic detector

Both n-i-p and p-i-n structures have been examined for the InSb photovoltaic detector. Absolute spectral responsivities of these detectors are given in the following. Both detector showed the photoresponse up to  $5.5\mu\text{m}$  at 77 K and  $7.5\mu\text{m}$  at 300 K. As is clearly seen from the graph, p-i-n structure gave responsivities almost two orders of magnitude higher than n-i-p structure. We think that in the n-i-p structure the p-n junction is closer to the substrate and this might result in the lower performance. When p-n junction is closer to the substrate side, the junction can have more defect density and at the same time the incident photon flux can be reduced by the absorption from the top n-type and intrinsic layer. Further study should be done to understand this results because it is important for the detector structure determination of the InTlSb photovoltaic detectors.

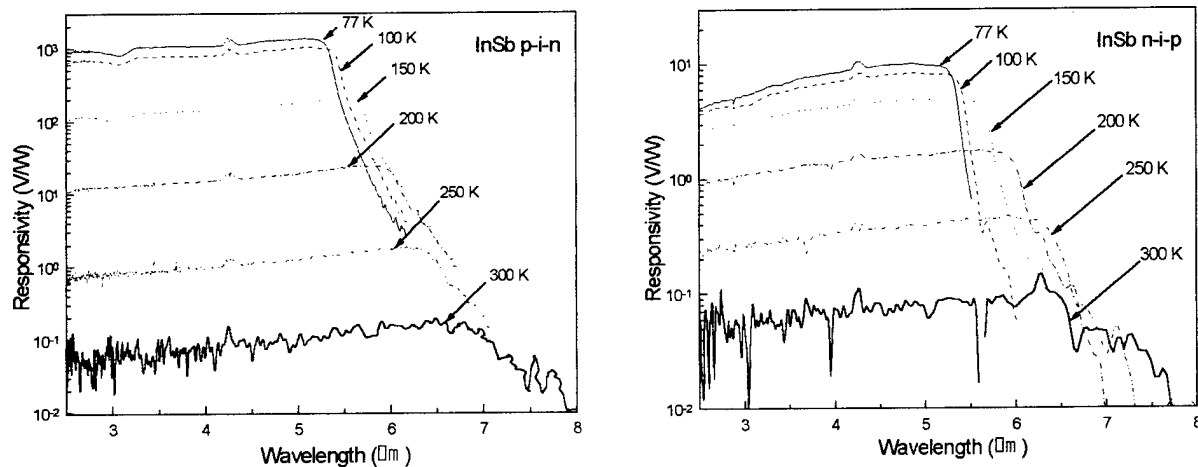


Figure 30: Photoresponse of InSb photodiodes with different structures (p-i-n and n-i-p).

### InAsSb photovoltaic detector

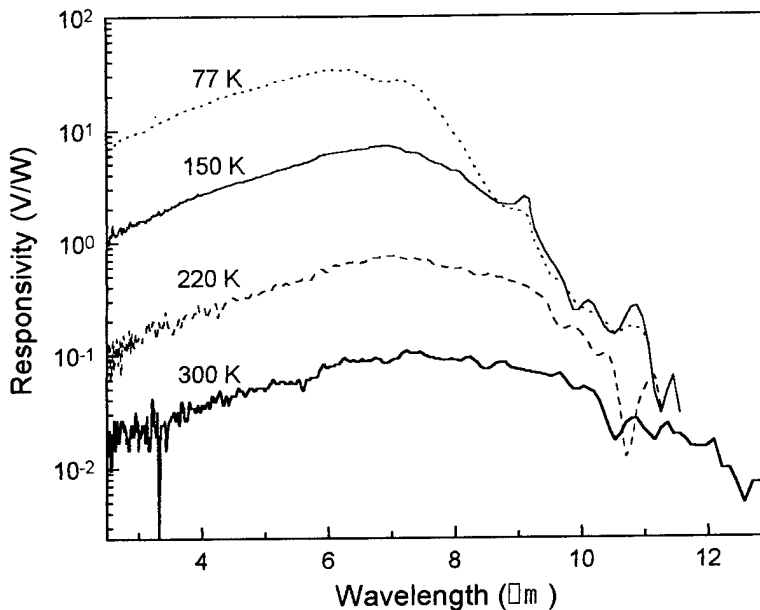


Figure 31: Photoresponse of p- $\pi$ -n InSb/InAs<sub>0.15</sub>Sb<sub>0.85</sub>/InSb double heterojunction photodiode.

As a first step for the longer wavelength photovoltaic detector applications, InAsSb was investigated first because it is well developed system. As InTlSb material system and the detector from it are expected to be similar to those from InAsSb, the investigation of InAsSb system is worth doing. At the same time InAsSb can make competition with HgCdTe for near room temperature operation at 8-12  $\mu\text{m}$  spectral range. Work performed at CQD showed well behaved InAsSb photodiode. p<sup>+</sup>-InSb/p<sup>-</sup>-InAs<sub>1-x</sub>Sb<sub>x</sub>/n<sup>+</sup>-InSb double heterojunction photodiodes operated at near room temperature in the 8-13  $\mu\text{m}$  region of infrared spectrum. A room temperature photovoltaic response of up to 13  $\mu\text{m}$  has been observed at 300 K with an  $x \approx 0.85$  sample as shown in Figure 31. The voltage responsivity-area product of  $3 \times 10^{-5}\text{Vcm}^2/\text{W}$  has been obtained at 300 K for the 10.6  $\mu\text{m}$  optimized device.

#### InTlSb photovoltaic detector

In order to approach the InTlSb photovoltaic detectors, InSb/InTlSb/InSb p-i-n double heterostructures were suggested. The doping level for the p-type contact layer was  $5 \times 10^{18}\text{cm}^{-3}$  and n-type layer was  $5 \times 10^{16}\text{cm}^{-3}$ . Almost same processing step as that for InSb detector has been used. Even though the surface of the layer was rough, Ti/Au metals made good contact with the surface. Wire bonding was achieved with Au-ball bonding machine but with more care than InSb case. The spectral response was obtained only up to 5.5  $\mu\text{m}$  indicating no response from the InTlSb layer.

## CONCLUSION

In this work, growth and material properties of InSb, InTlSb, and InTlP epitaxial films have been investigated and their potentials for infrared detection have been explored. High quality InSb films were grown on lattice mismatched GaAs and GaAs-coated Si substrates using TMI and TMSb as indium and antimony sources.

Reproducible growth of InTlSb has been achieved. Variation of Tl composition by changing the Tl flow or Sb flow has been obtained and InTlSb layers with different Tl compositions have been directly grown on semi-insulating GaAs substrate. Photoconductors have been fabricated by depositing Au/Ti on the edges of the rectangular shaped InTlSb samples. The detector performance has been measured. Corresponding calculation for the effective carrier lifetime ( $\tau$ ) and estimated detectivity ( $D^*$ ) resulted in the  $\tau$  of 10-50 ns and  $D^*$  of  $2\text{-}9 \times 10^8 \text{ cm}\cdot\text{Hz}^{1/2}/\text{W}$  at 77K. At 300 K,  $D^*$  was  $10^6\text{-}10^7 \text{ cm}\cdot\text{Hz}^{1/2}/\text{W}$  and  $\tau$  was 0.1-0.6 ns.

Photoconductivity measurements on InTlP/InP indicate an increase of the cutoff wavelength up to 8  $\mu\text{m}$  with increasing Tl incorporation. Recently, we have observed LWIR photoconductivity up to 15  $\mu\text{m}$  at room temperature by incorporating Tl into InAsSb.

Systematic doping studies have been done for InSb. Using DEZn lower p-type doping level of  $3 \times 10^{16} \text{ cm}^{-3}$  has been achieved. Similarity of doping characteristics for InAsSb and InTlSb have also been verified. Using the established growth techniques and doping level control, InSb and InAsSb photovoltaic detectors have been demonstrated. During the fabrication of those detectors, processing technology for the InSb based materials has also been developed. Preliminary InTlSb photovoltaic detector has also been fabricated.

Throughout this study we discovered the feasibility of various III-V semiconductors for the LWIR applications. They include InTlSb, InTlP, InTlAsSb, InAsSb, and InSbBi compounds. Because of their possibility to replace the current leading HgCdTe material system, the subject is very exciting and needs to be continued. The continuing work will be performed at the Center for Quantum Devices.

## **FUTURE WORKS**

1. Further extension of cutoff wavelength with increased Tl incorporation in InSb and InAsSb up to 20  $\mu\text{m}$ .
2. Optimization of device performance of room temperature operating 8-14  $\mu\text{m}$  InTlAsSb photoconductors.
3. Preliminary growth of p-n junction structure based on InTlSb and InTlAsSb.
4. Growth of InSb/InTlAsSb/InSb (InSb/InTlSb/InSb) double heterojunction p-i-n photovoltaic detectors for 8-12  $\mu\text{m}$  applications.

## SUMMARY of the PROJECT

1. Number of papers submitted to referred Journals but not published yet : 1
2. Number of papers published in referred Journals : 17
3. Number of books or chapters submitted but not yet published : 0
4. Number of printed technical reports and non-referred papers : 1
5. Number of patents filed : 3
6. Number of patents granted : 0
7. Number of invited presentations at workshops of professional society meetings : 5
8. Honors/awards/prizes for contract/grant employees : 1
9. Number of graduate students and post-docs supported at least 25% this year on contract grant : 6

### Graduate Students

- |            |          |
|------------|----------|
| Total :    | <u>3</u> |
| Female :   | <u>0</u> |
| Minority : | <u>0</u> |

### Post Docs

- |            |          |
|------------|----------|
| Total :    | <u>3</u> |
| Female :   | <u>0</u> |
| Minority : | <u>0</u> |

10. Number of female of minority PIs or CO-Pis:

- |                       |          |
|-----------------------|----------|
| New Female :          | <u>0</u> |
| Continuing Female :   | <u>1</u> |
| New Minority :        | <u>0</u> |
| Continuing Minority : | <u>0</u> |

11. Recent Graduates: 1

12. Technology Transfer : Personnel transfer (Dr. R. Sudharsanan doing similar work at SPIRE corporation)

## LIST OF PUBLICATIONS

- Y. H. Choi, R. Sudharsanan, C. Besicki, E. Bigan, and M. Razeghi, Mat. Res Soc. Symp. Proc. 281, 375, (1993).
- C. Besicki, Y. H. Choi, R. Sudharsanan, and M. Razeghi, J. Appl. Phys. 73, 5009, (1993).
- S. N. Song, J. B. Ketterson, Y. H. Choi, R. Sudharsanan, and M. Razeghi, Appl. Phys. Lett. 63, 964, (1993).
- Y. H. Choi, C. Besicki, R. Sudharsanan, and M. Razeghi, Appl. Phys. Lett. 63, 361, (1993).
- M. Razeghi, Y. H. Choi, P. T. Staveteig, and E. Bigan, Proceedings of the 184th Meeting of the Electrochemical Society, New Orleans, Louisiana, October, (1993).
- Y. H. Choi, G. Labeyrie, P. T. Staveteig, E. Bigan, and M. Razeghi, Proceedings of the 184th Meeting of the Electrochemical Society, New Orleans, Louisiana, October, (1993).
- Y. H. Choi, “InTlSb for 8-12 $\mu$ m range detector,” PhD qualifying exam, Northwestern university, Department of electrical engineering and computer science, (1993).
- Y. H. Choi, P. T. Staveteig, E. Bigan, and M. Razeghi, J. Appl. Phys. 75, (1994).
- E. Bigan, Y. H. Choi, G. Labeyrie, and M. Razeghi, Proceedings of SPIE, LosAngeles, California, (1994).
- P. T. Staveteig, Y. H. Choi, G. Labeyrie, E. Bigan, and M. Razeghi, Appl. Phys. Lett. 64, 460, (1994).
- M. Razeghi, Y. H. Choi, J. D. Kim, and E. Bigan, Electrochamical Society, Miami, Florida, October, (1994).
- M. Razeghi, “Organo-Metallic Vapor Phase Epitaxy of Semiconductors,” chapter in Handbook on Semiconductors, Second Edition, Volume3: Materials, Properties and Preparations.
- E. Michel, G. Singh, S. Slivken, C. Besicki, P. Bove, I Ferguson, and M. Razeghi, Appl. Phys. Lett., 65, 3338 (1994).
- G. Singh, E. Michel, C. Jelen, S. Slivken, J. Xu, P. Bove, I. Ferguson, and M. Razeghi, J. Vac. Sci. Technol. B, 13, 783 (1995).
- E. Michel, R. Peters, S. Slivken, C. Jelen, P. Bove, J. Xu, I Fergison, and M. Razeghi, Proceedings of the SPIE, 2397, 379 (1995)
- J. D. Kim, S. Kim, D. Wu, J. Wojkowski, J. Xu, J. Piotrowski, E. Bigan, and M. Razeghi, Appl. Phys. Lett. 67, 2645 (1995).
- M. Razeghi, J. D. Kim, S. J. Park, Y. H. Choi, D. Wu, E. Michel, J. Xu, and E. Bigan, Proceedings of the 22nd International Symposium on Compound Semiconductors, Cheju Island, Korea, 1085 (1995).

- J. D. Kim, D. Wu, J. Wojkowski, S. J. Park, Y. H. Choi, J. Xu, J. Piotrowski, and M. Razeghi, Proceedings of the 188th Electrochemical Society Meeting, Chicago, Illinois, October, (1995).
- J. D. Kim, D. Wu, J. Wojkowski, J. Piotrowski, J. Xu, and M. Razeghi, Appl. Phys. Lett. 68, 99 (1996).
- E. Michel, J. Xu, J. D. Kim, I. Ferguson, and M. Razeghi, IEEE Phot. Tech. Lett., 8, 673 (1996)
- E. Michel, J. D. Kim, S. Park, J. Xu, I Ferguson, and M. Razeghi, Proceedings of the SPIE, 2685, 105 (1996).
- E. Michel, J. D. Kim, J. Xu, I. Ferguson, and M. Razeghi, Appl. Phys. Lett. 69, 215, 1996.
- J. D. Kim, E. Michel, S. J. Park, J. Xu, S. Javadpour, and M. Razeghi, Appl. Phys. Lett. 69, 343, 1996.
- J. D. Kim, E. Michel, H. Mohseini, J. Wojkowski, J. J. Lee, and M. Razeghi, SPIE V2999, 55 1997.
- M. Razeghi, J. D. Kim, C. Jelen, S. Slivken, E. Michel, H. Mohseini, J. J. Lee, J. Wojkowski, K. S. Kim, H. I. Jeon, and J. Xu, IEEE-WOFE, V57 1997.
- M. Razeghi, J. D. Kim, J. J. Lee, E. Michel, H. Mohseini, , J. Wojkowski, J. Sandven, and J. Xu, ECS, Paris, 1997.
- J. J. Lee, J. D. Kim, and M. Razeghi, Appl. Phys. Lett. 70, 3266 1997.
- J. J. Lee, J. D. Kim, and M. Razeghi, Appl. Phys. Lett. 71, 2298 1997.
- J. J. Lee and M. Razeghi, Proc. SPIE 3287, 256 1998.
- J. J. Lee, J. D. Kim, and M. Razeghi, Appl. Phys. Lett. 73, 602 1998.
- J. J. Lee and M. Razeghi Opto-Electron. Rev. 6, 25 1998.
- M. Razeghi, J. Wojkowski, H. Mohseini, J. D. Kim, and J. J. Lee, Int. Phys. Cof. Ser 1998.
- J. J. Lee, J. D. Kim, and M. Razeghi J of Kor. Phys. Soc. (in press)
- J. J. Lee, J. D. Kim, and M. Razeghi Opto-Electron. Rev. (submitted for publication).